Jupiter's Atmospheric Composition and Cloud Structure Deduced from Absorption Bands in Reflected Sunlight

MAKIKO SATO AND JAMES E. HANSEN

NASA Goddard Institute for Space Studies, Goddard Space Flight Center, New York, NY 10025

(Manuscript received 2 March 1979)

ABSTRACT

The spectrum of sunlight reflected by Jupiter is analyzed by comparing observations of Woodman *et al.* (1979) with multiple-scattering computations. The analysis yields information on the vertical cloud structure at several latitudes and on the abundance of CH_4 and NH_3 in the atmosphere of Jupiter.

The abundance of CH_4 is $(1.8 \pm 0.4) \times 10^{-3}$ for $[CH_4]/[H_2]$, which corresponds to a carbon abundance 2 ± 0.4 times that in the atmosphere of the sun for currently accepted values of the solar composition. The quoted limits for the abundance include the effects of uncertainties in the cloud and haze structure. The abundance of NH_3 is $(2.8 \pm 1.0) \times 10^{-4}$ for $[NH_3]/[H_2]$ in the region between 1 bar and 3–5 bars, corresponding to a nitrogen abundance 1.5 ± 0.5 times that in the atmosphere of the sun. Thus nitrogen is at least as abundant on Jupiter as on the sun, and it may exceed the abundance in the solar atmosphere by a factor as great as that for carbon. These abundances suggest that all ices (and rocks) are overabundant on Jupiter by a factor approximately 2 or more, providing an important constraint on models for the formation of Jupiter from the primitive solar nebula.

Clouds of mean visible optical depth approximately 10 exist in both belts and zones at a pressure level of several hundred millibars. The pressure level of the clouds, the gaseous NH_3 abundance, the mean temperature profile and the Clausius-Clapeyron relation together suggest that these clouds are predominantly ammonia crystals and place the cloud bottom at 600–700 mb. Beneath this "ammonia" cloud region is an optically thick cloud layer at 3–5 bars; this cloud may be composed of H_2O. The region between these two cloud layers is relatively transparent. Thus NH_4SH clouds, assumed to be optically thick in all previous multi-layered cloud models for Jupiter, are optically thin or broken, if they exist.

A diffuse distribution of aerosols ("haze") exists between approximately 150 and 400–500 mb, i.e., above the main ammonia cloud region. These aerosols are at least 1 μm in diameter. The ultraviolet absorption occurs in both the haze region and the ammonia cloud region. The decreasing absorption with increasing wavelength is due to an increasing single scattering albedo rather than a decreasing aerosol optical depth as in the "Axel dust" model. Thus the spectral variation of albedo reflects a changing bulk absorption coefficient of the material composing the aerosols and is diagnostic of the aerosol composition.

Ratio spectra of the North Tropical Zone (NTrZ) and North Equatorial Belt (NEB) imply that the scatterers in the 150–500 mb haze region (which may include ammonia "cirrus") reach to higher altitudes over the NTrZ than over the NEB. But the tops of the more optically dense main "cloud" layer appear to reach to higher altitudes over the NEB, implying that the usual picture of the zones as regions of rising motions and enhanced ammonia cloudiness is too simple. The total optical thickness of aerosols in the haze and cloud regions is greater in the zone than in the belt, but there is more ultraviolet-absorbing aerosol in the belt. Ten parameters are needed to describe the vertical distribution of aerosol properties to satisfy only the spectra of Woodman *et al.*, suggesting that the atmospheric dynamics and cloud physics on Jupiter are extremely complex.

1. Introduction

Photographs of Jupiter, such as the high-resolution images obtained by the Pioneer 10 and 11 flyby spacecraft, provide remarkable detail on the horizontal structure of the clouds covering the planet. However, the vertical structure of the clouds and their composition must still be inferred indirectly. Current ideas about the clouds of Jupiter are based to a large extent on theoretical considerations of cloud formation in an atmosphere in thermochemical equilibrium, with refinements based on attempts to model the spectrum of radiation scattered or emitted by the planet.

Fig. 1 shows the cloud layers predicted by Lewis (1969a,b) and Weidenschilling and Lewis (1973) on the assumption that the chemical composition of Jupiter is the same as that of the sun. The upper three cloud layers are NH_3, NH_4SH and H_2O, with the cloud bottoms at ~0.6, 1.6 and 4.5 bars, respectively, if we employ the current temperature profile of Orton (1977). Danielson and Tomasko (1969)

0022-4928/79/071133-35$12.75

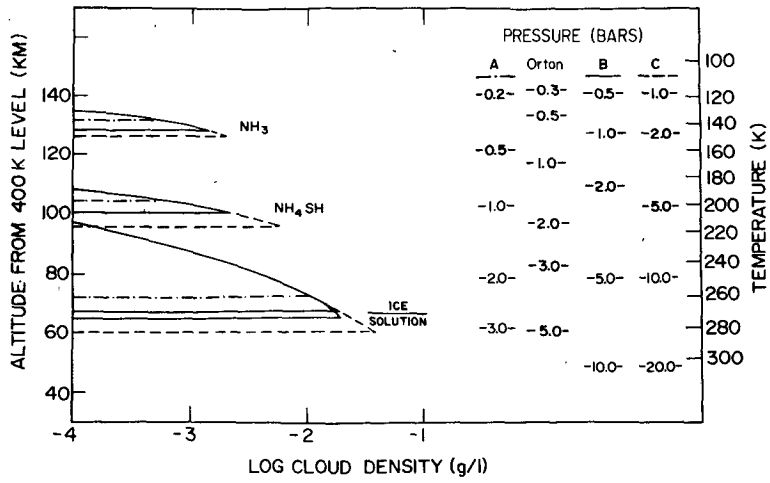

FIG. 1. Cloud profiles for three assumed pressure-temperature profiles for a solar-composition Jupiter (after Weidenschilling and Lewis, 1973). Temperatures are nearly the same for all three models. We also illustrate the recent pressure-temperature profile of Orton (1977), which falls between models A and B.

suggested a two-cloud model for interpreting the observed spectra of Jupiter, with an ammonia cloud of finite optical thickness at $T \approx 145$ K ($P \approx 0.5$ bar) and an NH_4SH cloud of effectively infinite optical thickness at $T \approx 210$ K ($P \approx 2$ bars). With this model they were able to get consistent abundances for H_2 from the S(1) quadrupole line at ~6367 Å in the 4-0 absorption band and from the 3-0 band at ~8150 Å. Danielson and Tomasko recognized that they may have been able to achieve that same consistency with a one-cloud model, with a diffuse distribution of scatterers which permit photons in a weak absorption line such as the S(1) line in the 4-0 band to penetrate more deeply into the atmosphere and thus "see" a larger amount of gas, but they rejected such a model on the basis that the mean free-scattering path (>1 km) would be much larger than that for terrestrial clouds. The latter argument is not convincing, particularly since we now know that the mean free path in the visible clouds on Venus is several kilometers (Hansen and Hovenier, 1974; Lacis, 1975).

Since the work of Danielson and Tomasko (1969) most models used for detailed analysis of observations have been either a two-cloud model with an optically thin cloud at a pressure of several hundred millibars and an optically thick cloud at $P \approx 2$ bars (Axel, 1972; Bergstralh, 1973(a); Hunt, 1973a,b; Hunt and Bergstralh, 1977), or a diffuse cloud model with a large mean free photon path, in some cases with gas above the clouds (Fink and Belton, 1969; Bergstralh, 1973(a); Teifel, 1976). One significant modification of the Danielson-Tomasko model which has proved necessary is the addition of a UV absorbing haze above the ammonia clouds in order to match the decreasing albedo of Jupiter into the ultraviolet (Axel, 1972); this haze is commonly referred to as "Axel dust".

More recent analyses (e.g., Cochran, 1977; Wallace and Smith, 1977) are still unable to definitively choose between a two-cloud model or a diffuse cloud. Wallace and Smith feel that the two-cloud model of Danielson and Tomasko (1969) should be rejected on the grounds that (according to Wallace and Smith) its upper cloud would have to be at a pressure (200–300 mb) which is too low to be identified with ammonia. However, Wallace and Smith do not entirely solve the problem of how to obtain consistent abundances from the visible and near-infrared methane bands, and they admit the need to also analyze the H_2 bands.

Our approach in this paper is to analyze the principal H_2, CH_4 and NH_3 bands and to ask what can be said about the cloud properties from the criteria that a single model must work for all of these bands. We do not assume the existence of any cloud on the basis of thermochemical equilibrium considerations. We compute the theoretical spectra with a multiple-scattering method we have developed (Sato *et al.*, 1977) which permits rapid computations for an atmosphere of arbitrary vertical inhomogeneity. Our computations are restricted to an atmosphere with plane-parallel layers. Although a large amount of consideration has been given to the possibility of cloud towers or other small-scale horizontal inhomogeneities (Squires, 1957; Appleby and van Blerkom, 1975), we argue that the effect of horizontal inhomogeneities on the analysis can be minimized by relying primarily on observations near the center of the planetary disk.

In Section 2 we present information about atmospheric properties required for the modeling and analysis of observed spectra. Section 3 defines a hierarchy of models of increasing complexity, ranging from the simple 1-parameter reflecting-layer model to the 6-parameter two-cloud model; we mention the observations used to determine the best-fitting parameters and include some indication of why the simplest models prove inadequate, based on the computations in later sections. Sections 4–6 contain comparisons of model computations with H_2, CH_4 and NH_3 absorption features, respectively. In Section 7 we examine observations sensitive to the cloud tops and the aerosols at higher altitudes; this section includes analysis of ratio spectra of a belt and a zone to determine differences of cloud and aerosol properties between these regions. In Section 8 we perform several checks on our analyses, including tests of certain assumptions in the computations, e.g., with regard to the phase function of the cloud particles. The analysis of several different observations inevitably requires some back and fourth considerations between different sections. In summarizing our conclusions in Section 9, we try to give some indication of how firm the different conclusions are, and we emphasize the significance of the information on gas abundances with regard to the formation of the planets and the significance of the cloud and aerosol structure with regard to atmospheric dynamics.

2. Atmospheric properties

a. Gaseous composition and Rayleigh scattering

As a standard case for comparison we initially use the solar elemental abundances for the atmosphere of Jupiter. Table 1 shows this standard composition, based on abundances of Ross and Aller (1976) and Lambert (1978). The mean molecular weight of this mixture is $\tilde{\mu} = 2.3$.

The Rayleigh scattering coefficient for a mixture of gases is given by Eq. (2.25) of Hansen and Travis (1974). We employ the gaseous refractive indices given by Allen (1963) and the depolarization factors given by Penndorf (1957).

TABLE 1. Standard atmospheric composition.

Constituent	Solar abundance: Ross and Aller	Solar abundance: Lambert	Standard fraction
H_2	1.00	1.00	0.886
He	1.26×10^{-1}	—	0.112
CH_4	8.34×10^{-4}	9.36×10^{-4}	7.86×10^{-4}
NH_3	1.74×10^{-4}	1.95×10^{-4}	1.64×10^{-4}
H_2O	1.38×10^{-3}	1.66×10^{-3}	1.35×10^{-3}

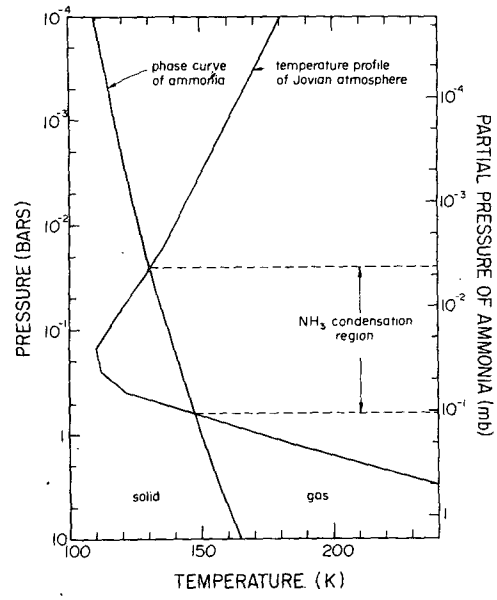

FIG. 2. Temperature profile of Jovian atmosphere employed in our computations and phase diagram of ammonia. The pressure scales are matched for the standard case (Table 1), in which the abundance $[NH_3]/[H_2]$ for Jupiter is taken as being equal to 2[N]/[H] in the atmosphere of the sun. This case leads to the indicated region where ammonia would condense.

The optical thickness due to Rayleigh scattering is related to the atmospheric pressure by (Hansen and Travis, 1974)

$$\frac{d\tau_R}{dP} = \frac{\sigma_R}{g\tilde{\mu}}, \tag{1}$$

where g is the acceleration of gravity and $\sigma_R = k_R/N$ is independent of pressure and temperature. Taking $g = 2322$ cm s^{-2}, the Rayleigh optical thickness above $P = 1$ bar is $\tau_R = 0.009\lambda^{-4}(1 + 0.015\lambda^{-2})$ with λ in micrometers. As a convenient reference, note that for $\lambda = 0.55$ μm this yields $\tau_R \approx 0.10$ at $P = 1$ bar, which is the same as for the Earth (Hansen and Travis, 1974).

b. Temperature profile and ammonia condensation

We employ the nominal temperature profile of Orton (1977), which is shown in Fig. 2. The temperature at $P = 1$ bar is 171.2 K.

Fig. 2 includes the phase curve of ammonia, given by the Clausius-Clapeyron equation

$$\log P = -\frac{1630}{T} + 7.122, \tag{2}$$

where P is in bars; the constants in (2) are taken from the *International Critical Tables* (1928). The standard atmospheric composition of Table 1 is used to relate the two pressure scales, i.e., the ratio of abundances $[NH_3]/[H_2]$ on Jupiter is assumed to be

equal to 2[N]/[H] on the sun. For that composition ammonia would condense between the indicated levels. At altitudes where the assumed composition and temperature imply supersaturation, we reduce the ammonia abundance to the saturation value for our model atmosphere computations.

In the stratosphere of Jupiter we take the mixing ratio of NH_3 to be constant and equal to its value at the tropopause. NH_3 (and CH_4) may be further depleted in the stratosphere by photolysis. However, the amount of gas at these levels is too small to significantly influence the spectra which we compute, and hence it is not essential to account for such depletion.

c. Cloud particle phase functions

We make most of our computations for a particular phase function, and then indicate in Section 8 the extent to which the results depend on the phase function. In fact, since we minimize reliance on observations of the angular distribution of scattered light, the results for one phase function can be scaled to apply approximately to another phase function. The similarity relations depend upon the anisotropy parameter $\langle\cos\alpha\rangle$, which is the mean cosine of the scattering angle weighted by the phase function.

In most of our computations we use the phase function of Kawabata and Hansen (1975), i.e.,

$$\log P(\alpha) = \begin{cases} \log P_0 + A\left(\alpha - \dfrac{\pi}{2}\right) & \text{for} \quad 0 \leq \alpha \leq \dfrac{\pi}{2} \\ \log P_0 & \text{for} \quad \dfrac{\pi}{2} \leq \alpha \leq \pi \ . \end{cases} \tag{3}$$

The two constants are determined by the normalization of $P(\alpha)$ and by specifying the desired anisotropy parameter. On the basis of analysis of the linear polarization, Kawabata and Hansen (1975) conclude that the particles in the visible Jupiter clouds are large and nonspherical, suggesting that the phase function is independent of wavelength and that an appropriate anisotropy parameter is 0.80–0.85, including the effects of a diffraction peak. The diffraction peak can be handled by treating the photons scattered in this peak as being unscattered and scaling $\langle\cos\alpha\rangle$ and the single-scattering albedo $\tilde{\omega}$ appropriately (Hansen, 1971). Thus we choose $\langle\cos\alpha\rangle = 0.65$ for most of our computations, leading to $A = -1.21$ and $P_0 = -0.205$. This phase function is shown in Fig. 3. Other phase functions employed for the Jupiter clouds are also illustrated in Fig. 3.

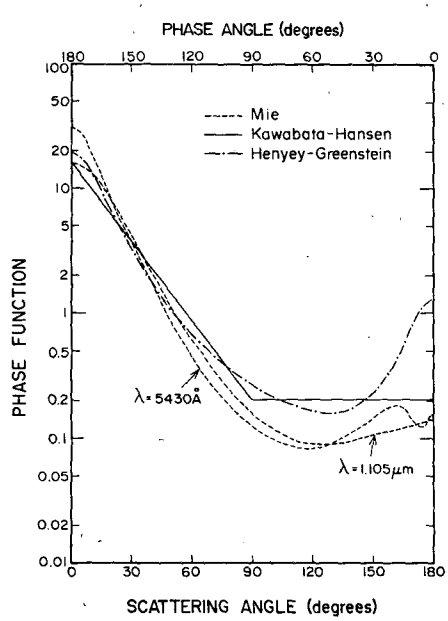

FIG. 3. Several phase functions employed for the Jupiter cloud particles. $\langle\cos\alpha\rangle$ is 0.65 for the phase function of Kawabata and Hansen (1975), 0.65 for the two-term Henyey-Greenstein phase function of Cochran (1977), and 0.787 and 0.756 at $\lambda = 5430$ Å and $\lambda = 1.105$ μm for the Mie phase functions of Morozhenko and Yanovitskii (1973).

d. Other definitions

The phase function for a mixture of cloud particles and gas is

$$P(\alpha) = (1 - f)P_{cl}(\alpha) + fP_R(\alpha), \tag{4}$$

where P_R and P_{cl} are the Rayleigh and cloud particle phase functions, f is the fraction of the total scattering coefficient accounted for by molecular scattering, i.e.,

$$f = \frac{k_R}{k_{s,cl} + k_R}, \tag{5}$$

k_R is the Rayleigh scattering coefficient and $k_{s,cl}$ the cloud particle scattering coefficient. The single-scattering albedo is

$$\tilde{\omega} = \frac{k_{s,cl} + k_R}{k_{s,cl} + k_R + k_{a,cl} + k_\nu} = \frac{\tilde{\omega}_c}{1 + \dfrac{k_\nu}{k_c}}, \tag{6}$$

where k_ν is the gaseous absorption coefficient, $k_{a,cl}$ the cloud particle absorption coefficient and $\tilde{\omega}_c$ the single-scattering albedo in the continuum.

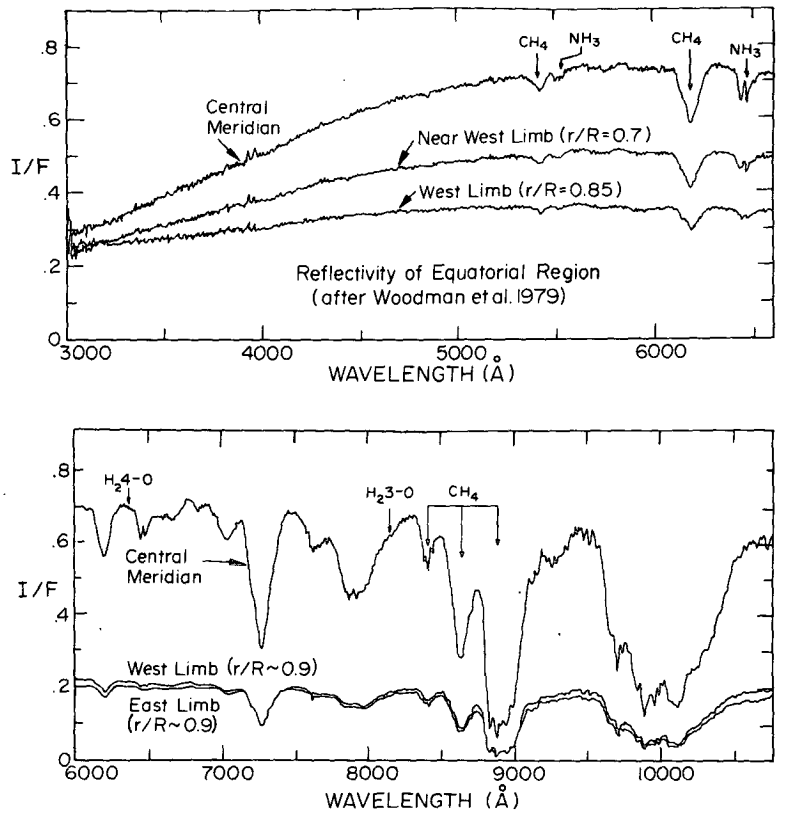

FIG. 4. Reflectivity of the ER observed by Woodman *et al.* (1979).

3. Cloud models

We consider a wide range of models beginning with the simplest idealizations, the standard reflecting layer model (RLM) and the homogeneous cloud model (HCM). Eventually, based on consideration of observations discussed in Sections 4–7, we are forced to accept a much more complex model with three scattering layers: an optically thin haze in the upper troposphere, an ammonia cloud of finite optical thickness at a pressure level of several hundred millibars, and an optically thick cloud at a depth of several bars.

Our approach is to first analyze spectra of reflected solar radiation, ignoring any preconceived ideas about the cloud structure based on considerations of thermochemical equilibrium, interpretations of other observations such as thermal infrared fluxes, or current models for the atmospheric dynamics. In Sections 8 and 9 we compare the resulting model with models for the Jovian clouds suggested by other investigators.

Our analysis is primarily of spectra obtained by Woodman *et al.* (1979) for the region 3000 Å to 1 μm. Fig. 4 shows their observed reflectivity for the Equatorial Region (ER).[1] We also analyze their observations of the North Tropical Zone (NTrZ) and the North Equatorial Belt (NEB). We use the observations of strong and weak methane bands, ammonia bands and continua regions including the ultraviolet. The only additional data we need is the equivalent width of the hydrogen quadrupole line, for which we use the observations discussed in Section 4. The fact that we are able to rely primarily on a single data set minimizes the effect of temporal variability on Jupiter, as well as uncertainties that would arise from different seeing conditions, telescope characteristics or fields of view, if we had to combine several data sets. Prior to the availability of the Woodman *et al.* data we did, in fact, perform a similar analysis using a collection of different data sets. The model deduced, with an upper level haze, an ammonia cloud layer and a

[1] The term Equatorial Region seems more appropriate than Equatorial Zone, since that region does not have the visual appearance of either a belt or zone. In addition, the spectra of Woodman *et al.* (1979) for the ER are more like the NTrZ than the NEB for short wavelengths ($\lambda < 6000$ Å), but more like the NEB than the NTrZ for long wavelengths ($\lambda > 6000$ Å).

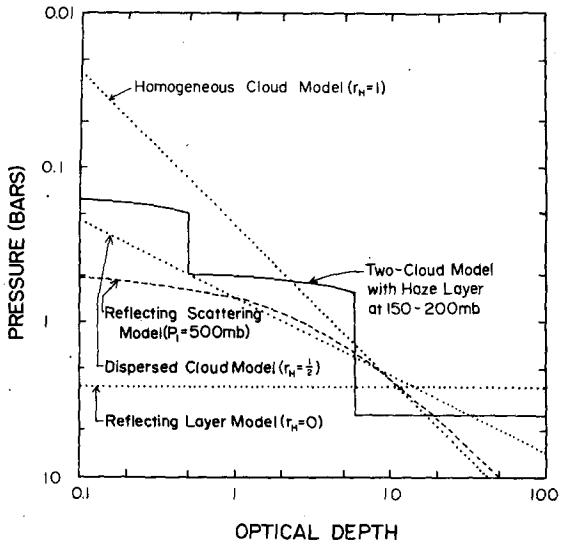

FIG. 5. Optical depth of clouds as a function of pressure for several cloud models. r_H is the ratio of the cloud opacity and gaseous atmosphere scale heights.

second cloud layer at a depth of several bars, was basically similar to that which we report here, as were the abundances of CH_4 and NH_3. However, with the Woodman *et al.* data we are now able to remove major caveats from that analysis and provide more precise model parameters.

In all of the cloud models we assume that the cloud optical depth is independent of wavelength for the region 3000 Å to 1 μm. For this to be sufficiently accurate it is only necessary that the cloud particles not be smaller than about 1 μm. This assumption is not made *a priori* for the haze layer introduced in Section 7.

Fig. 5 shows the cloud optical depth above a given pressure level for several specific cloud models. We discuss these models briefly in this section, beginning with the simplest idealizations, the RLM (1 parameter) and HCM (2 parameters).

The RLM has an opaque Lambert surface of reflectivity R_{cl} at the cloud-top pressure level P_{cl}. We choose the value of R_{cl} to yield the observed continuum reflectivity at the center of each zone or belt. An observed equivalent width is then used to yield the gas abundance above the cloud for this model. Except for the usually small effect of Rayleigh scattering, the abundance derived from the RLM is independent of R_{cl}, and hence it is essentially a 1-parameter model.

The HCM has a uniform mixture of cloud particles and gas molecules. The two parameters are $\tilde{\omega}_{cl}$ and f_R, the ratio of the molecular (Rayleigh) scattering coefficient to the total scattering coefficient at some wavelength, which we take to be $\lambda = 3650$ Å. For a specified cloud particle phase function, the single-scattering albedo is determined from the observed reflectivity in the continuum. An observed equivalent width can then be used to obtain the specific abundance of absorbing gas. An H_2 line, with an assumption about the percentage of He present, yields the Rayleigh fraction f_R.

Analysis of observations with the simple RLM and HCM yields useful information for guiding construction of more realistic models, even though neither of these models is consistent with all observations. The RLM yields grossly inconsistent methane abundances from weak and strong methane bands. The HCM does not have this problem but it is inconsistent with the observed variation of equivalent widths from the center to the limb of the planet. As the next step in complexity we consider two 3-parameter models: the dispersed cloud model (DCM) and the reflecting scattering model (RSM).

In the DCM the cloud particles have a scale height which in general is different from that of the gaseous atmosphere and is specified by r_H, the ratio of the cloud particle scale height to the molecular scale height. The three parameters describing the model are thus r_H, $\tilde{\omega}_{cl}$, and the ratio of cloud particle and Rayleigh extinction coefficients at any specified pressure level. The DCM is a physically plausible model for a hazy atmosphere; it gives a good representation for many remote observations of Venus (Lacis, 1975).

The RSM is a 3-parameter model which is a combination of the RLM and the HCM. It has pure gas above the pressure P_1 and a homogeneous cloud beneath that level. The parameters are P_1, $\tilde{\omega}_{cl}$ and f_R. The RSM has been considered for Jupiter by Teifel (1976), Cochran (1977) and Wallace and Smith (1977).

For the two 3-parameter models, the DCM and the RSM, the continuum reflectivity and the H_2 4-0 equivalent width can be used to determine two of the three parameters. We can choose as the temporarily undetermined parameters, r_H, the ratio of scale heights in the DCM, and P_1 the pressure at the cloud top in the RSM, in order to achieve the intended flexibility for each of these models. Thus, as r_H is permitted to vary from 0 to 1, the DCM varies from the RLM to the HCM; values of $r_H > 1$ are also permissible. Similarly, as P_1 varies from some maximum value to zero, the RSM also varies from the RLM to the HCM, but in a way which is quite different than for the DCM.

A third independent observation is needed to specify the third parameter in either the DCM or the RSM. One procedure we use is to examine the strength of CH_4 bands. This introduces the CH_4 abundance as another parameter to be determined, but by using observations in two spectral regions which differ substantially in the average depth of photon penetration, it is possible to both establish

the final cloud model parameter and determine the methane abundance (for that model).

As an alternative procedure we also use the center-to-limb variation (CTLV) of the equivalent width of an absorption band to specify the third parameter in these models. This has the advantage of restricting the analysis to a single spectral region, thus avoiding uncertainties in the spectral variation of the continuum albedo. A major disadvantage of using the CTLV is that horizontal inhomogeneities or thin high altitude hazes may complicate the interpretation; this difficulty is alleviated to some extent by not relying on observations very near the limb, thus assuring that the different observations refer to roughly similar depths in the atmosphere.

We find that neither the DCM nor the RSM provides an adequate fit to both the observed variation of CH_4 equivalent widths with band strength and the observed CTLV of absorption bands.

As the next stage of complexity we choose the two-cloud model (TCM). Rationale for this type of model is provided by observed CTLV's which suggest gas above a cloud layer and by simultaneous consideration of observed CH_4 and NH_3 equivalent widths, which suggests the need for a clear space beneath the upper cloud (Section 5). There are six basic parameters in the TCM, as indicated in Fig. 6: P_1, P_2 and P_3, which are the pressures at the top and bottom of the upper cloud and the top of the lower cloud, $\tilde{\omega}_{cl}$, τ_{cl} and R_3, which is the reflectivity of the lower cloud. Two-cloud models have been considered extensively for Jupiter (e.g., Danielson and Tomasko, 1969; Axel, 1972; Bergstralh, 1973a; Hunt, 1973a,b; Cochran, 1977; Wallace and Smith, 1977; West, 1978). The original TCM, that of Danielson and Tomasko (1969), was based on the cloud structure predicted by Lewis (1969a,b) with a finite ammonia cloud at several hundred millibars pressure and an optically thick NH_4SH cloud at ~2 bars. The subsequent investigators have employed basically the same structure, although Wallace and Smith (1977) question whether the upper cloud should be identified with ammonia since their analysis suggests that it occurs at about the 200 mb level. Most of these investigators, in addition to fixing the level of one or both of the clouds *a priori* have made other assumptions to eliminate model parameters, for example, by approximating the upper cloud as an infinitely thin reflecting and transmitting sheet (i.e., without any multiple scattering or gaseous absorption within the cloud).

In our analysis we initially consider all six parameters as being unknowns to be determined by analysis of the observed spectra, particularly from the strengths of H_2, CH_4 and NH_3 absorption lines. The NH_3 observations are found to indicate that the upper cloud layer is ammonia, thus permitting specification of the level of the cloud bottom for a given NH_3 abundance. Although ammonia particles would be practically nonabsorbing at most wavelengths, a significant amount of absorption could be provided by "impurities". Therefore we consider the full range of possibilities from $\tilde{\omega}_{cl} = 1$ to $R_3 = 1$. In order to obtain consistent gas abundances from observations in different spectral regions, it is found that a second cloud deck is required at the 3–5 bar level. On the basis of observations which are primarily sensitive to the outer skin of the atmosphere, we also conclude that there is an optically thin haze above the upper cloud layer. Models for the haze are discussed in Section 7.

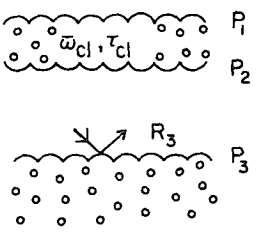

FIG. 6. Schematic illustration of the 6 parameters in our version of the two-cloud model.

4. Hydrogen quadrupole lines

We consider H_2 observations first, since we use them as a barometer for determining pressure levels. Each of the models described in the previous section is capable of providing agreement with the H_2 observations at the center of the disk, but this results in certain constraints on the parameters defining each model. These constraints are then included in the computations in the following sections on methane and ammonia absorption bands.

a. Laboratory data

1) LINE STRENGTHS

The temperature dependence of the strengths of the $v - 0$ $S(J)$ quadrupole lines is taken as

$$S_{vJ}(T) = A_{vJ} \frac{g_J \exp(-E_{0J}/kT)}{Q_r(T)}, \qquad (7)$$

where v and J are vibrational and rotational quantum numbers. The rotational partition function Q_r is given by

$$Q_r(T) = \sum_J g_J \exp[-BJ(J+1)hc/kT]. \qquad (8)$$

The constants in (7) and (8) are given by Herzberg (1950).

Prior to laboratory measurements of the 4-0 $S(1)$ line strength discussed below, there were two methods employed to estimate its value. In the first method, the theoretical expression for the line strength was used based on the theoretical

TABLE 2. Hydrogen quadrupole line strengths at 300 K [10^{-4} cm^{-1}(km-am)$^{-1}$].

Line	Wavelength (Å)	Theoretical		Experimental		
		Birnbaum and Poll (1969)	Poll and Wolniewicz (1978)	Rank *et al.* (1966)	Bergstralh *et al.* (1978)	Trauger *et al.* (1978)
3-0 $S(0)$	8272.71	3.4	—	—	—	—
3-0 $S(1)$	8150.75	13	14.4	13	—	14.1 ± 1.4
3-0 $S(2)$	8046.64	2.4	—	—	—	—
4-0 $S(1)$	6367.29	1.6	1.76	0.9	0.88 ± 0.32	0.95 ± 0.14

quadrupole matrix elements calculated by Birnbaum and Poll (1969); this yielded the line strength[2] 1.6×10^{-4} cm^{-1} (km-am)$^{-1}$ at $T = 300$ K. Recent calculations of Poll and Wolniewicz (1978) give a similar result. In the second method, line strengths measured by Rank *et al.* (1966) for the 1-0, 2-0 and 3-0 bands were extrapolated to the 4-0 band; this yielded a 4-0 line strength of 0.9×10^{-4} cm^{-1} (km-am)$^{-1}$. Owen and Mason (1968) tried both of these values and found that, with their reflecting layer model, the theoretical value based on Birnbaum and Poll yielded an H_2 abundance consistent with that obtained from the 3-0 line, while the value based on the measurements of Rank *et al.* did not. Owen and Mason thus preferred the value 1.6×10^{-4} cm^{-1} (km-am)$^{-1}$ for the 4-0 line strength. Subsequently, Danielson and Tomasko (1969) and others employed the same value in their analyses.

Recently Bergstralh *et al.* (1978) and Trauger *et al.* (1978) independently measured the line strength of the 4-0 $S(1)$ line and obtained $S_{4,1}(297\text{ K}) = 0.88 \pm 0.32 \times 10^{-4}$ cm^{-1} (km-am)$^{-1}$ and $S_{4,1} \times (294\text{ K}) = 0.95 \pm 0.14 \times 10^{-4}$ cm^{-1} (km-am)$^{-1}$, respectively. Table 2 summarizes the different values for the H_2 quadrupole line strengths. In our model atmosphere calculations we take $S_{3,1}(300\text{ K}) = 1.3 \times 10^{-3}$ cm^{-1} (km-am)$^{-1}$ and $S_{4,1}(297\text{ K}) = 0.92 \times 10^{-4}$ cm^{-1} (km-am)$^{-1}$. We will show that these values actually lead to consistent values for the H_2 abundance. We also discuss in Section 8 how our final results depend on the assumed H_2 line strength.

2) LINE WIDTHS

Fink and Belton (1969) pointed out that the H_2 quadrupole lines are affected by collision narrowing since the pressure broadening of those lines is extremely small [cf. Dicke (1953) and Galatry (1961)].

We employed the subroutines of Herbert (1974) to compute the Galatry line shape, using a pressure-broadening coefficient $K = K_0(P/P_0)(T_0/T)^{3/4}$ and a self-diffusion coefficient $D = D_0(P_0/P)(T/T_0)^{3/2}$, where $P_0 = 1$ bar, $T_0 = 273$ K, $K_0 = 0.00164$ cm^{-1} and $D_0 = 1.34$ cm^2 s^{-1} (James, 1969).

The pressure shift predicted by McKellar (1974) and verified by Bergstralh *et al.* (1978) is taken into account, although it was found to have little effect on the computed equivalent width of the line. The shift (cm^{-1}) of an H_2 quadrupole line of the v-0 band was assumed to be

$$\Delta\nu(\rho,T) = v\rho(A + BT + CT^2), \qquad (9)$$

where $A = -0.0123$, $B = +4.78 \times 10^{-5}$, $C = -4.78 \times 10^{-8}$, and ρ is the H_2 density in amagats.

b. Planetary observations

The observed equivalent widths of H_2 3-0 $S(J)$ lines and the 4-0 $S(1)$ line on Jupiter are summarized in Table 3. There is substantial spread in the observed equivalent widths for the 3-0 lines, which are overlapped with water vapor absorption in the terrestrial atmosphere. The 4-0 equivalent width seems reasonably well established at $W = (8 \pm 1)$ mÅ in the ER, with only moderate variations over the disk. We have averaged the observations of Cochran *et al.* (1976) separately for the NEB and STrZ, obtaining values of 8.3 and 7.3 mÅ, respectively. The belt-zone difference found by Carleton and Traub (1974) for the NEB and SEZ is qualitatively similar, but only about half as large (cf. Table 3). Both the 3-0 and 4-0 lines probably have significant time variations (Carleton and Traub, 1974; Hunt and Bergstralh, 1977).

c. Model computations

In our computations we take [He]/[H_2] as 0.13, the same as in the sun's atmosphere. The uncertainty of this ratio for Jupiter (Hunten, 1976) is sufficiently small that it should not substantially limit our conclusions. We rely primarily on the 4-0 observations, because of the wide variations in 3-0 results from one observer to another and the difficulty in defining the continuum for the 3-0 line, but we check our conclusions for consistency with the 3-0 observations.

In most of our computations for the H_2 4-0 band we employed a reflectivity of 0.71 for the ER (Fig. 4).

[2] Units involve the amagat (am), a measure of abundance (moles cm^{-3} at STP).

TABLE 3. Observed equivalent widths of H_2 quadrupole lines on Jupiter (mÅ).

Observers	3-0 S(0)	3-0 S(1)	4-0 S(1)
Zabriskie (1962)		80	
Spinrad and Trafton (1963)	31	28 (ER) 40 (CM)	8.0 ± 2.0
Beckman (1967)			6.0 ± 2.5
Owen and Mason (1968)		49 ± 6 (CM)	8.5 ± 1.5 (CM)
Fink and Belton (1969)	45 ± 8	71 ± 8 (ER)	9 ± 2
Emerson *et al.* (1969)			7.8 ± 1.2
Trafton (1972)		53 ± 2 (ER)	
Trauger *et al.* (1973)			8.1 ± 0.2
Carleton and Traub (1974)		35–50 (SEZ)	8.2 ± 0.2 (SEZ) 8.7 ± 0.4 (NEB) 8.6 ± 0.3 (GRS) 8.5 ± 0.5 (ER)
Cochran *et al.* (1976)			7.3 ± 1 (STrZ) 8.3 ± 1 (NEB)
Hunt and Bergstralh (1977)	min. 22.4 ± 2.9 max. 45.9 ± 3.0	34.5 ± 5.0 62.6 ± 2.2	4.5 ± 0.7 12.5 ± 1.4

In checking the consistency of the abundance determined from the 3-0 observations with that from the 4-0 band, we illustrate results for ER reflectivities ranging from 0.63 to 0.70 for the continuum at the 3-0 band, because the extent of consistency between the two bands depends on the relative continuum levels in the two spectral regions.

For the RLM we obtain an H_2 abundance of 105 km-am, based on a band strength $S_{4,1}(297\ \mathrm{K}) = 0.92 \times 10^{-4}\ \mathrm{cm}^{-1}\ (\mathrm{km\text{-}am})^{-1}$ and an assumed equivalent width $W = 8$ mÅ at the disk center. This corresponds to a "surface" pressure of $P_{cl} = 2.7$ bars for the standard composition (Table 1). The value obtained for P_{cl} varies almost linearly with W/S, a result which can be used to estimate the change in P_{cl} for different assumed values of W and $S_{4,1}$. The difference in equivalent widths, measured by Cochran *et al.* (1976) for the NEB and STrZ, corresponds to $\Delta P_{cl} \approx 300$ mb, with the reflecting level at a smaller pressure (higher altitude) in the zone. The largest belt-zone difference measured by Carleton and Traub (1974), between the NEB and SEZ, corresponds to $\Delta P_{cl} \approx 150$ mb.

For the HCM we obtain a continuum single-scattering albedo $\tilde{\omega}_{cl} = 0.9931$ and a specific abundance $a = 8.8$ km-am for the ER with the Kawabata-Hansen phase function; the mean free photon path between scatterings by the cloud particles is $\sigma_{cl}^{-1} = 6$ km at $P = 1$ bar. With this model the zone-belt variations in specific abundance are as large as 30–40%, with the values in the belts being larger primarily as a result of lower continuum reflectivity. With isotropic scattering the results for the ER are $\tilde{\omega}_{cl} = 0.98$ and $a = 25$ km-am, based on use of similarity relations.

For the DCM there is a continuum of models, differing primarily in the value for the scale height ratio r_H, consistent with the H_2 4-0 equivalent width at the disk center. If, for example, we choose $r_H = \frac{1}{2}$, which gives reasonable agreement with the CTLV for 6190 Å CH_4 band (see Section 5), we obtain $\tilde{\omega}_{cl} = 0.9934$ and $\tau_{cl} = 1$ at $P \approx 700$ mb for the ER with the Kawabata-Hansen phase function. For the RSM there is also a continuum of models fitting the H_2 equivalent widths. If we choose $P_1 = 500$ mb, we obtain $\tilde{\omega}_{cl} = 0.9933$ and $a = 7.2$ km-am. These two models are considered further in the following sections on methane and ammonia absorption bands.

For the TCM which we are eventually led to, the H_2 4-0 equivalent width serves as a constraint effectively determining one parameter. As an example, we illustrate in Fig. 7 computations for a particular version of the TCM. In this case P_2 was 0.63 bars (appropriate for ammonia clouds if NH_3 is of solar abundance) and the single-scattering albedo was specified as $\tilde{\omega}_{cl} = 1$ (also appropriate for an ammonia cloud); the location of the cloud bottom and the cloud particle single-scattering albedo are examined in later sections. R_3 was chosen to yield the observed reflectivity ($I_c/F = 0.71$) at the disk center in the continuum near the H_2 4-0 line. Results

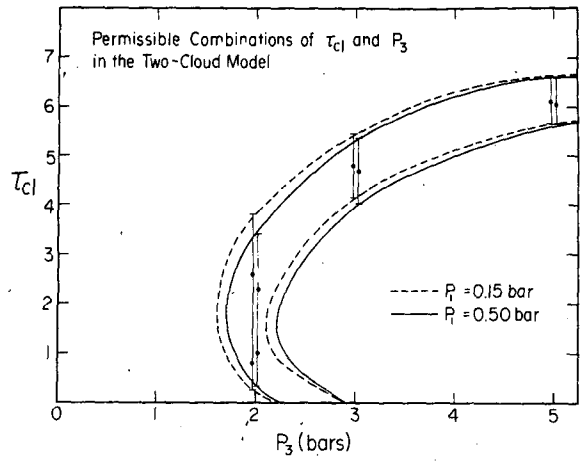

FIG. 7. The region between the extreme curves specifies the combinations of P_3 and τ_{cl} in the two-cloud model (TCM) which yield $W = 8.0 \pm 1.0$ mÅ for the H_2 4-0 $S(1)$ line in the ER. τ_{cl} must be multiplied by 2 to include the effect of the expected diffraction peak in the cloud particle phase function. The results refer to the version of the TCM with conservative scattering in the upper cloud ($\tilde{\omega}_{c1} = 1$); absorption in the upper cloud increases τ_{cl}. These calculations were for $P_2 = 630$ mb, but the results are not sensitive to the uncertainties in that parameter. In subsequent calculations each version of the TCM investigated is subjected to the constraint to agree with the observed H_2 equivalent width.

are shown for two different values of P_1—0.15 bars, corresponding to the upper cloud extending to the tropopause, and 0.5 bars, corresponding to a relatively thin region of clouds. The remaining two parameters, τ_{cl} and P_3, can not both be determined from the observed equivalent width for the H_2 4-0 line, so we are left with a family of acceptable combinations of τ_{cl} and P_3, as illustrated in Fig. 7. The two closely spaced curves indicate the uncertainty in the $\tau_{cl} = P_3$ relation due to lack of knowledge of P_1. The spread between the two pairs of curves is due to the uncertainty in the measured equivalent width of the 4-0 $S(1)$ line, $W = 8.0 \pm 1.0$ mÅ. For example, Fig. 7 means that P_3 must be at least 1.7 bars, and if we can choose either P_3 or τ_{cl} from some other observations, that will essentially determine the remaining parameter. In fact, based on CH_4 observations, we find $P_3 \approx 3$–5 bars, implying[3] that $\tau_{cl} \approx 4.5$–6.

As a check, it is useful to see whether the same model yields agreement with the observed equivalent width of the 3-0 $S(1)$ line. Fig. 8 shows the 3-0 equivalent width as a function of P_3, or equivalently as a function of τ_{cl}. For the case $\tau_{cl} = 0$, which corresponds to the RLM, the 3-0 equivalent width is indeed larger than most of the observations, if the H_2 abundance derived from the 4-0 equivalent width (Fig. 7) is used; this agrees with a conclusion of Owen and Mason (1968). However, Fig. 8 also shows that with the TCM the expected equivalent widths are in reasonable agreement with the observations for the cloud optical thickness (5–6) determined from CH_4 and NH_3 observations (cf. following sections). As is illustrated, the results depend significantly on the reflectivity assumed for the continuum near the H_2 3-0 line. Because of the uncertainty in the continuum albedo and the variation in the 3-0 equivalent width from one observer to another, we do not rely on this line for providing quantitative information on the atmospheric structure. Part of the variation in measured equivalent widths may be due to real time variations in the atmospheric structure. It is thus highly desirable to have simultaneous measurements of the H_2 equivalent widths and the spectral reflectivity.

We examined the effect of the pressure shift of the H_2 line (discussed above) on the equivalent width and line profile. Fig. 9 compares the line profiles with and without the pressure shift for the TCM with $P_1 = 500$ mb, $P_2 = 630$ mb and $P_3 = 5$ bars. The equivalent width is unaffected within 0.2%. A small asymmetry is introduced in the profile, but observations of Jupiter are not sufficiently accurate to reveal this.

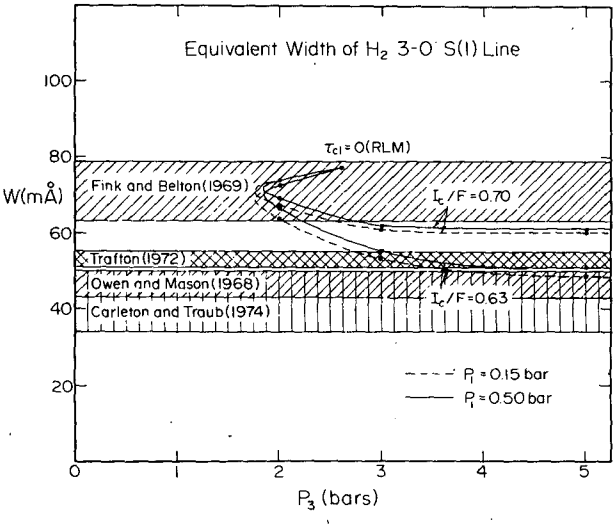

FIG. 8. Equivalent width of 3-0 $S(1)$ line for the combinations of P_3 and τ_{cl} in the TCM which yield $W = 8.0$ mÅ for the 4-0 $S(1)$ line (cf. Fig. 7). Results are shown for two values of P_1 (150 and 500 mb) and two values of the continuum reflectivity (0.63 and 0.70). The terminal point ($\tau_{cl} = 0$) of the above curves is the result for the RLM. The curves were generated from computations for several values of τ_{cl} (solid dots), approximately $\tau_{cl} = 1$, 2.5, 4.7 and 6. For the HCM (not illustrated) $W = 63$ mÅ if $I_c/F = 0.70$, while $W = 57$ mÅ if $I_c/F = 0.63$. The observations are specified in Table 3.

[3] The computations were made using the Kawabata-Hansen phase function. Thus, in the probable case that the cloud particles are larger than the wavelength, we must multiply τ_{c1} by 2 to allow for diffraction, implying that the actual cloud optical thickness is ~10. The equivalent isotropic scattering optical thickness is ~2.

Finally, we also looked at the center-to-limb variation (CTLV) of the H_2 equivalent width in observations (e.g., Cochran *et al.*, 1976). The observed equivalent width has relatively little systematic variation except near the limbs where it increases significantly. This is inconsistent with the HCM, which yields a monotonically decreasing equivalent width, but all of the other models can be made to be reasonably consistent with the observations. We do not rely on the H_2 CTLV data to specify model parameters, because measurements simultaneous with the Woodman *et al.* (1979) spectra are not available. However, a similar type of information can be obtained from the CTLV of CH_4 bands, which is examined in the following section.

In summary, the H_2 observations provide the capability to establish one parameter in any model for the vertical atmospheric structure, and the continuum reflectivity determines a second parameter. There is weak evidence from the H_2 observations alone that neither the RLM nor the HCM is appropriate for Jupiter. However, to obtain detailed information on the atmospheric structure it is necessary to consider the H_2 data along with other observations.

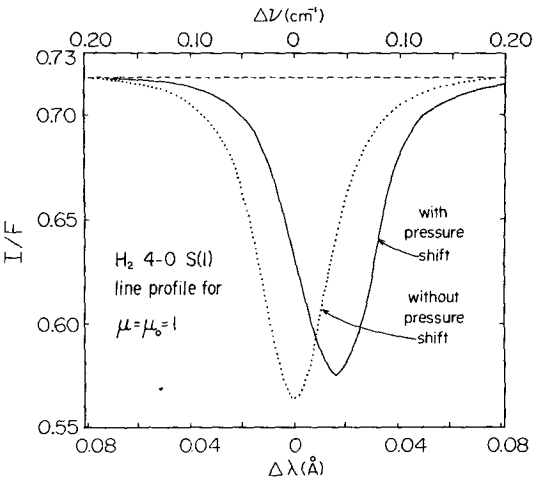

FIG. 9. Profiles of the H_2 quadrupole 4-0 $S(1)$ line at $\mu = \mu_0 = 1$. One profile is computed without consideration of the pressure shift, the other with it. Both profiles are for the TCM with $P_3 = 5$ bars, $P_2 = 700$ mb, $P_1 = 150$ mb and $\tau_{cl} = 6.0$.

5. Methane bands

We next consider methane, since it should be in the gaseous state at the temperatures and pressures in the Jovian atmosphere and homogeneously mixed with the bulk of the other gases. The methane abundance can thus be specified by a single number, say the ratio of methane and hydrogen number densities, which can be determined for a given model by matching an observed CH_4 equivalent width. Since there are available observations of both weak and strong methane bands, we expect to be able to obtain at least one parameter describing the vertical cloud structure in addition to obtaining the methane abundance.

Most investigators have used the strong $3\nu_3$ band at 1.1 μm and/or the weak visible bands to infer the CH_4 abundance. We choose instead to first examine methane bands of different strength within the 8500–8900 Å region (cf. Fig. 4). This allows us to 1) use data taken at the same time and with the same instrument in comparing bands of different strengths, 2) avoid assumptions about how the cloud and aerosol optical properties may change over a broad spectral interval, and 3) use a single continuum for the strong and weak bands, avoiding the major uncertainty in the definition of the continuum in the $3\nu_3$ region. As a result we can precisely determine model parameters and the methane abundance. However, we then also verify that the same models which yield a well-defined methane abundance for the 8500–8900 Å region also solve the problem of obtaining consistent results from the weak visible and strong $3\nu_3$ bands.

As a secondary constraint on the models we examine the CLTV of the methane absorption. This provides some information about the vertical structure in the cloud-top region, despite uncertainties about horizontal variations which surely exist in the cloud structure.

a. Laboratory data

Lutz *et al.* (1976) measured the strengths of the methane bands at 4410, 4860, 5430 and 5760 Å, with results shown in their Table 2 and their Figs. 3–5. These bands are weak and pressure-independent for column densities up to 1 km-am.

Dick and Fink (1977) obtained laboratory spectra covering the region from 4200 Å to 1.06 μm, which were used by Fink *et al.* (1977) with the Goody random band model to obtain absorption and pressure coefficients at intervals of 10 Å. They found that for the conditions in the visible levels of the Jovian atmosphere these can be used directly without the necessity of line-by-line integration.

Giver (1978) measured the intensities and profiles of the CH_4 bands in the region 4350 Å to 1.06 μm with high resolution (0.5–0.6 Å). Giver was able to employ large methane abundances (20 km-am) and control thermal gradients in the laboratory apparatus. Thus in the one area in which the above measurements showed a significant difference we employ Giver's results;

this is in the 5000 Å region where Giver (1978) and Lutz *et al.* (1976) are in good agreement but differ from Dick and Fink (1977). For the 8900 Å region, where the above measurements are in good agreement, we use the absorption coefficients and pressure coefficients of Fink *et al.* (1977); the band model parameters of Fink *et al.* (1977) are used with the k-distribution method described in Section 6, with five k values at each wavelength of interest. For the 6190 Å CH_4 band and shorter wavelengths the absorption was assumed to be a continuum (cf. Lutz *et al.*, 1976).

For the R-branch of the $3\nu_3$ band at 1.1 μm, which consists of J-manifolds of blended lines, we used a Lorentz line shape for each line with pressure broadening coefficient $\gamma_0 = 0.075$ cm^{-1} at $T = 295$ K and $P = 1$ atm and with the central frequencies measured by Maillard *et al.* (1973). We took the temperature dependence of the absorption strength of the J-manifold as

$$S_J(T) = S_J(T_0)\left(\frac{T_0}{T}\right)^{3/2} \times \exp\left[-\frac{BhcJ(J+1)}{k}\left(\frac{1}{T}-\frac{1}{T_0}\right)\right] \quad (10)$$

with $B = 5.24$ cm^{-1}, based on laboratory measurements by Margolis and Fox (1969) and corrections by Bergstralh and Margolis (1971).

b. Planetary observations

We primarily use the observations of Woodman *et al.* (1979) taken on 9 November 1976 at phase angle 2°. All three regions they observed (ER, NEB, NTrZ) were well defined and were resolved by their entrance aperture of 2.33 arc seconds by 2.48 arc seconds. Their resolution was ~8 Å for their blue spectra (3000–6600 Å) and ~16 Å for their red spectra (6000–10760 Å). Their red spectra were obtained on the central meridian and near both limbs. Their blue spectra were obtained on the central meridian, near the west limb and at an intermediate position. They estimate the absolute uncertainty in their reflectivities as 8–10% with much smaller uncertainties in the relative reflectivities.

c. Atmospheric models

We employ the models described in Section 3. For each model we include the constraint that it yield the observed equivalent width for the 4-0 $S(1)$ hydrogen quadrupole line (Section 4). We first compare the model reflectivities with observations for wavelengths of weak and strong absorption in the 8900 Å CH_4 band. In order for a model to be consistent with both the weak absorption at 8490 Å and the strong absorption at 8910 Å, the resulting curve should pass through the intersection of the observational bars in Fig. 10.

Fig. 10a illustrates the results for the simple models. The RLM cannot yield a consistent methane abundance; the 8490 Å region results in an abundance about a factor of 4 larger than that indicated by the 8910 Å region. This discrepancy in CH_4 abundance deduced from strong and weak bands with the RLM was first pointed out by Lutz *et al.* (1976) in reference to the 4860 and 5430 Å visible bands and the $3\nu_3$ band at 1.1 μm. On the other hand, the HCM is almost in agreement with the observations, with a methane abundance approximately a factor of 2 larger than present estimates for solar composition. The reason the HCM works is that scattering within the cloud permits a longer photon path length for a weaker absorption band. The results for the DCM with r_H between 0 and 1 fall between those for the RLM and HCM. The results for the RSM also fall between those for the RLM and HCM, as expected.

Although the HCM is consistent with the observed data in Fig. 10, that model is excluded by the CTLV of methane absorption as discussed below. The CTLV requires there to be a few hundred millibars of gas above the upper cloud, a conclusion which is independent of uncertainties about horizontal inhomogeneities in the cloud structure. As a result, none of the simple models is consistent with the observations.

The results for the simple models suggest how the vertical structure should be altered in order to obtain consistent abundances from the weak and strong CH_4 bands. There must be sufficient scattering at high levels (above ~1 bar) to prevent photons in the strong band from "seeing" too much CH_4, yet a substantial number of photons in the weak band must be allowed to penetrate to relatively great depths. This places a requirement on the transparency of the atmosphere beneath the level probed by the strong band. In fact, since the CTLV demands that there be relatively little scattering in the upper few hundred millibars the simple models indicate that the region at depth (beneath ~1 bar) must be freer of scatterers (compared to the 0.3–1 bar region) than in a homogeneous model. Thus there are requirements for 1) substantial scattering somewhere between a few hundred millibars and about one bar, 2) a clearer region beneath this, and 3) substantial scattering from some layer beneath the clear region, in order for the absorption in the weak band to appear in the reflection spectrum.

We are thus forced to something like the TCM as the next simplest model to try. We show in Section 6 that there must be ammonia condensa-

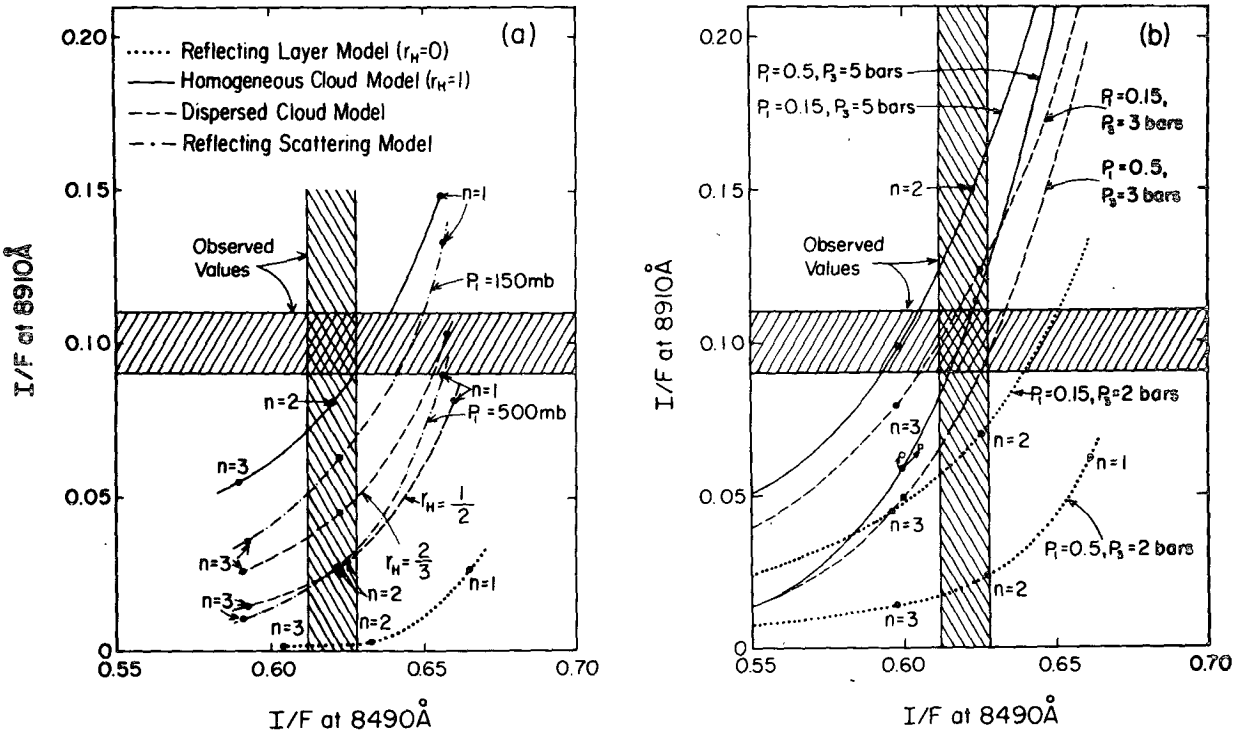

FIG. 10. Reflectivity at 8490 Å (weak band) and 8910 Å (strong band). Observations are by Woodman *et al.* (1979). (a) shows the simple models. The RLM has P_{cl} = 2.7 bars. The HCM has a specific abundance of 8.8 km-am of H_2. The DCM has r_H = ½ and r_H = ⅔, which result is the τ_{cl} = 1 level occurring at P = 680 and 480 mb, respectively. The RSM has P_1 = 500 mb and 150 mb which result in specific abundances of 7.0 and 8.2 km-am of H_2, respectively. n is the $[CH_4]/[H_2]$ ratio in units of 9×10^{-4}; thus n = 1 corresponds to current knowledge of C abundance in the solar atmosphere. (b) shows the results for the TCM for several combinations of the cloud-top levels, P_1 and P_3. In each case the bottom of the upper cloud is at P_2 = 630 mb. For P_3 = 2 bars there are two values of τ_{cl} consistent with the observed H_2 equivalent width (cf. Fig. 7), thus four cases for the two assumed values of P_1. The two cases illustrated for P_3 = 2 bars are the extreme cases. The open circle and open square show how a particular point is moved when isotropic and two-term Henyey-Greenstein phase functions are used (cf. Section 8).

tion in the upper of the two regions in which substantial scattering is required. Furthermore the gaseous ammonia abundance deduced from the ammonia bands accurately specifies the bottom of the region of ammonia condensation as 630–700 mb. Therefore in the most straightforward version of the TCM, which we employ in this section, we place the bottom of the upper cloud at 630 or 700 mb. We usually take $\tilde{\omega}_{cl} = 1$ in this cloud layer for $6000 \lesssim \lambda \lesssim 9000$ Å. The cloud particles may actually have a small amount of absorption, and thus in Section 7 we quantitatively examine the effect of possible cloud particle absorption.

Fig. 10b shows that both P_1 and P_3, the pressures at the tops of the two cloud layers, affect the ability of the model to match the observed intensities in the strong and weak methane bands. However, P_3 must be at least 3 bars. This conclusion is made stronger by the fact the CTLV in the methane bands indicate that P_1 is larger than 150 mb, and is probably in the range 350–550 mb; this range for P_1 is confirmed by analysis of ratio spectra in Section 7.

The above results imply that P_3 is 3–6 bars, which is substantially larger than in previous models. We therefore examine this aspect in greater detail. Fig. 11 reveals that we obtain similar constraints on P_3 when we examine methane bands of different strength. This figure also shows that the uncertainty in the absolute continuum does not basically modify the results. The variation in I_c/F which we examined is larger than the uncertainty stated by Woodman *et al.* (1979). It is also explicitly indicated in Fig. 11 that τ_{cl} changes with P_3. This is in response to the constraint that each model fit the observed equivalent width of the hydrogen quadrupole line. The indicated values of τ_{cl} must be multiplied by 2 to account for diffraction. Therefore our conclusions that P_3 is ~3–6 bars implies that τ_{cl} is about 10. This value for τ_{cl} is an effective optical thickness for the plane-parallel approximation. In reality there must be some areas in the ER which have greater optical thickness and some with smaller τ_{cl}, such as to give the transmission computed for a plane-parallel layer with $\tau \approx 10$. Because of the way the transmission increases with increasing τ, the actual

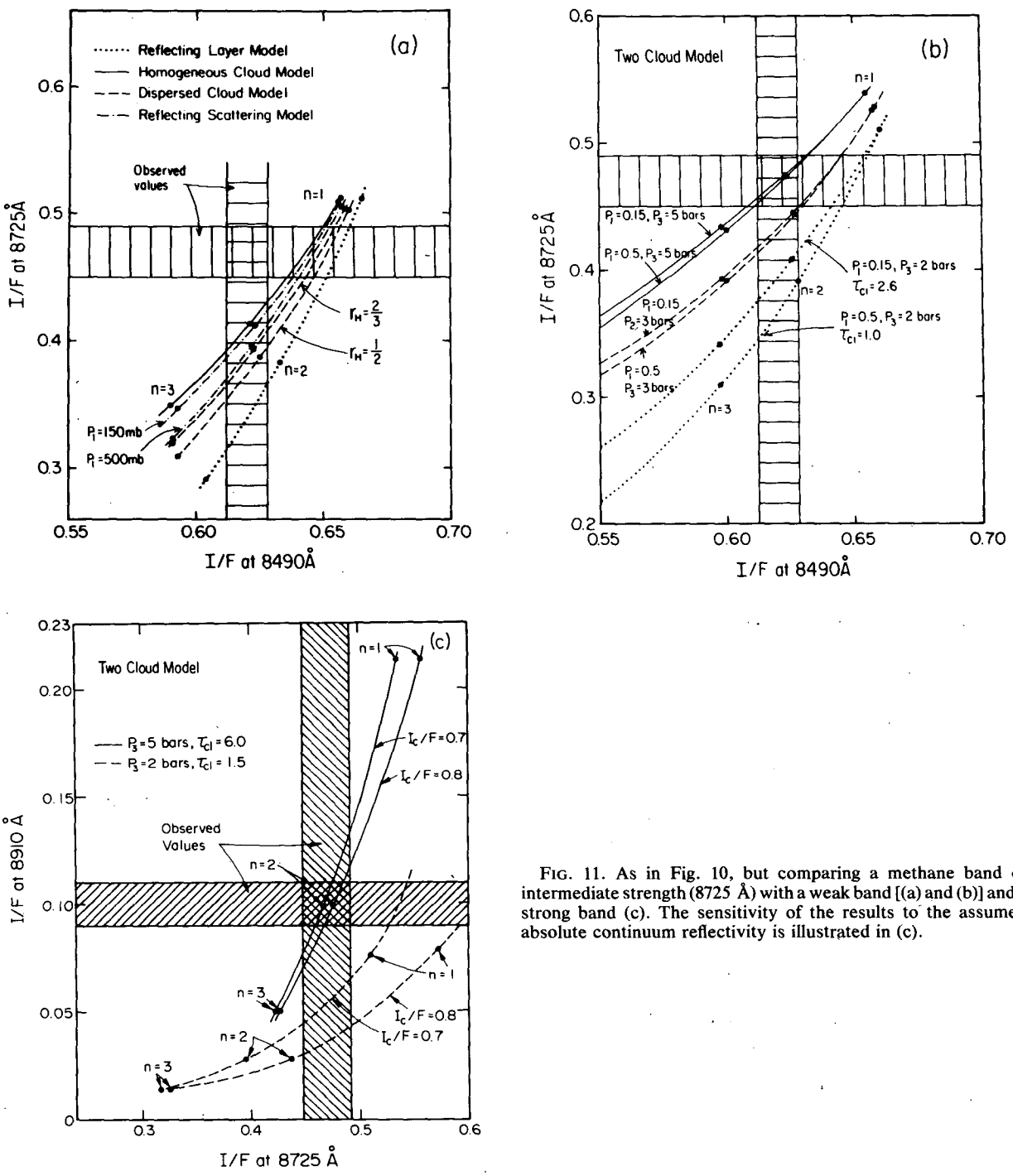

FIG. 11. As in Fig. 10, but comparing a methane band of intermediate strength (8725 Å) with a weak band [(a) and (b)] and a strong band (c). The sensitivity of the results to the assumed absolute continuum reflectivity is illustrated in (c).

area-weighted mean optical depth may be considerably greater than 10.

Before obtaining the observations of Woodman *et al.* (1979) we performed analyses similar to those above, but for the visible and the $3\nu_3$ bands. Although those data were less well suited for precise interpretation, for reasons stated at the beginning of this section, they yielded conclusions basically similar to those above. Since other investigators have concentrated on the $3\nu_3$ and visible bands, we show results for these bands in Fig. 12 for the TCM. This earlier study also lead to the conclusion that the lower cloud occurs at about the 5-bar level and $[CH_4]/[H_2] \approx 0.0018$.

It has been suggested to us that P_3 in our TCM is so large that pressure broadening of individual

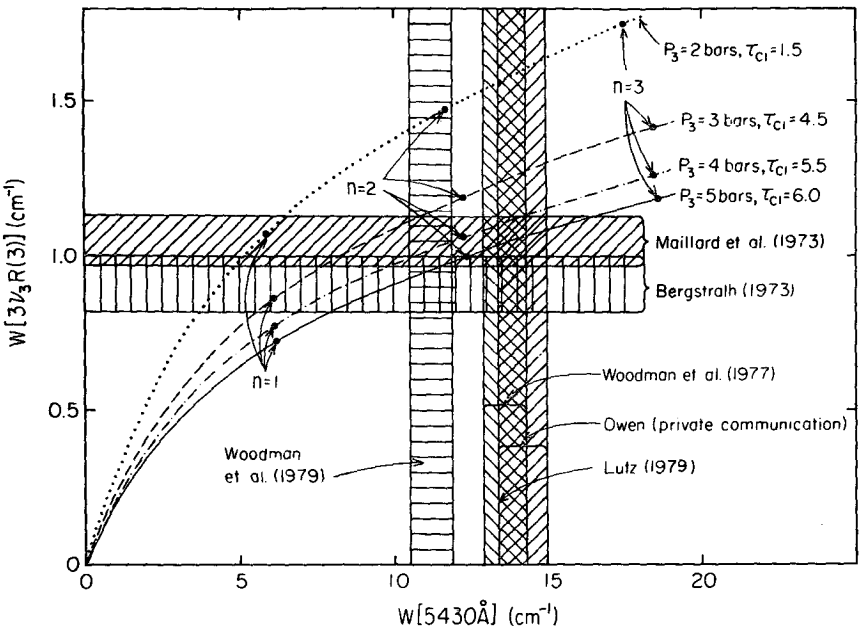

FIG. 12. Equivalent width of the 5430 Å and $3\nu_3$ methane bands. The computations are for the TCM with $P_1 = 500$ mb, $P_2 = 700$ mb and $\bar{\omega}_{cl} = 1$. I_c/F was taken as 0.7 for 5430 Å and 0.6 for the $3\nu_3$ band. The equivalent width of the $3\nu_3$ line was integrated over a 5 cm^{-1} interval. The breadth of observational bars indicates either the observer's quoted error or the spread for multiple observations.

$3\nu_3$ lines should produce much broader lines than are observed. Therefore, we computed $3\nu_3$ line profiles, convolved them with the instrumental profile of Bergstralh (1973) and compared them to his observations. Fig. 13 illustrates that the model lines have a width similar to that which is observed.

Finally, we briefly indicate the nature of the CTLV of the methane absorption for different models, since this has been a prime diagnostic in many of the past analyses of Jovian cloud structure. In this section we graph the CTLV in the manner usually employed. Because of the slant path for the direction of incident radiation (θ_0) and the viewing angle (θ), the CTLV data are primarily indicative of structure in the upper parts of the clouds and above the clouds. Therefore, in Section 7, where we are specially concerned with the structure in this part of the atmosphere, we examine the CTLV of methane absorption in greater depth with a technique employing the results for all band strengths.

Figs. 14a and 14b show the CTLV of the 6190 Å CH_4 band, while Figs. 14c and 14d show the CTLV of the strong 8900 Å band. Note that the equivalent width is illustrated for the 6190 Å band and the intensity relative to the continuum at 8910 Å; thus the observations show that absorption decreases toward the limb in the weak band and increases toward the limb in the center of the strong band. The falloff of absorption toward the limb at 6190 Å is opposite to the behavior for the RLM. However the observed falloff is not as steep as for the HCM, suggesting the need for a few hundred millibars of gas above the top cloud. The TCM is nearly in agreement with the observed CTLV, provided that the cloud top is at a sufficient depth ($P_1 \approx 500$ mb). The fact that the observed points based on Woodman *et al.*'s (1979) blue spectra (open circles) are systematically higher than the model is not a problem, since the most appropriate comparison is the relative CTLV not the absolute value. There is a very weak suggestion of the need for some scattering above the 500 mb level. We illustrate the effect on the CTLV of a haze layer of optical depth 0.5 at 150–200 mb. If this haze is distributed uniformly throughout the region 150–500 mb, its optical depth must be about twice as large to obtain a comparable effect.

The CTLV in the strong 8900 Å band is more sensitive to the possible need for a high-level haze layer. The observations have a rather flat CTLV, in spite of the strength of the methane absorption. Fig. 14 shows that this could be produced by a haze layer at 150–200 mb above a cloud top at 500 mb, but also by distributing the top cloud with a scale height about 40% as large as that for the gaseous atmosphere. A similar result is obtained with the cloud top at 500 mb and a uniform haze of optical depth unity between 150 and 500 mb.

The CTLV depends to a significant extent on the shape of the phase function. All of the results

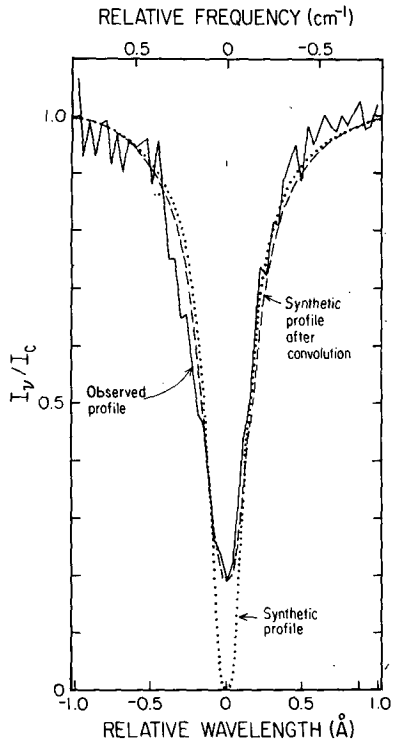

FIG. 13. $R(1)$ line profile of $3\nu_3$ methane band. Observation is from Bergstralh (1973b). Computation is for the TCM with $P_1 = 500$ mb, $P_2 = 700$ mb, $P_3 = 5$ bars, $\tilde{\omega}_{cl} = 1$, $\tau_{cl} = 6$ and $R_3 = 0.3$. The computed result is shown for infinite resolution and after being convolved with the instrumental broadening function given in Fig. 2 of Bergstralh (1973b). The local continuum for the models is taken as the computed intensity at $\Delta\nu = 1$ cm^{-1} from the line center, which is 95% of the intensity at $\Delta\nu = \infty$.

in Fig. 14 employ the Kawabata-Hansen phase function for both the clouds and haze. Interpretation of the observed CTLV is also hampered by uncertainties in pointing and smearing by atmospheric seeing conditions (cf. Section 7). Therefore, we do not attempt here to draw any detailed conclusions about the structure of the cloud tops and the haze above it. In Section 7 we make a more thorough analysis of the problem.

All of the results illustrated in this section are for the ER. However, the basic conclusions, with regard to the ability of the simple models and the TCM to fit the observed spectra and with regard to the methane abundance, apply equally well to the NTrZ and NEB. The spectra for all three regions are basically similar, but by analyzing the ratio of the spectra for different regions it is possible to extract significant information on how the clouds differ between belts and zones. This is also done in Section 7.

6. Ammonia bands

Absorption bands of ammonia exist throughout the spectrum of solar radiation reflected by Jupiter. The bands in the ultraviolet, where penetration is limited by Rayleigh scattering, and in the near infrared, where penetration is limited by strong gaseous absorption, refer to levels where the ammonia abundance is reduced by condensation (Fig. 1). However, the $5\nu_1$ band at 6450 Å and the even weaker band at 5510 Å are in regions of the spectrum where it should be possible to see to depths beneath the level of ammonia condensation.

a. Laboratory data and band model

Lutz (1979) measured the absorption coefficient of the 6450 and 5510 Å bands with 2 Å resolution, obtaining total band intensities of 0.63 ± 0.03 cm^{-1} (m-am)$^{-1}$ and 0.096 cm^{-1} (m-am)$^{-1}$, respectively, which we employ in our computations. These are in good agreement with the measurements of Giver *et al.* (1975 and private communication) which yielded 0.66 ± 0.06 cm^{-1} (m-am)$^{-1}$ and 0.08 cm^{-1} (m-am)$^{-1}$, respectively. Rank *et al.* (1966) measured the H_2 pressure broadening coefficients for 18 lines in the 6450 Å band, obtaining an average $2\gamma = 0.175$ cm^{-1} which we use for all lines in that band. To compute the equivalent widths of the 6450 and 5510 Å NH_3 bands we use the correlated k-distribution method of Lacis and Wang (1979). In this method the integration over frequency is replaced by integration over the probability distribution function $F(k)$ for absorption coefficients, which changes with pressure and temperature. $F(k)$ is obtained analytically from measured quantities by employing the Malkmus band model. This band model has a distribution of line intensities of the form $(C_1/S)\exp(-S/C_2)$, where C_1 and C_2 are constants. If we let S_B be the total band intensity, σ the mean line strength, a the abundance of the gas, $\delta = \Delta\nu/N$ the mean line spacing, the average transmission is given by

$$\bar{T} = \exp\left\{-\frac{\pi}{2}y\left[\left(\frac{4}{\pi}\frac{ka}{y}+1\right)^{1/2}-1\right]\right\}, \quad (11)$$

where the effective line strength is

$$k = \frac{\sigma}{\delta} = \frac{S_B}{\Delta\nu} \quad (12)$$

(cf. Goody, 1964; Malkmus, 1967). For the effective line width y we use

$$y = 0.25\,\frac{P}{P_0}\left(\frac{T_0}{T}\right)^{1/2} \text{ [cm}^{-1}\text{]}, \quad (13)$$

based on the pressure broadening coefficient of Rank *et al.* (1966) and a line spacing $\delta = 0.3$ cm^{-1}, where $P_0 = 1$ bar and $T_0 = 273$ K. We use this value of y for both the 6450 and 5510 Å bands. However, both bands are weak, and we have verified that the equivalent widths are not sensitive to y.

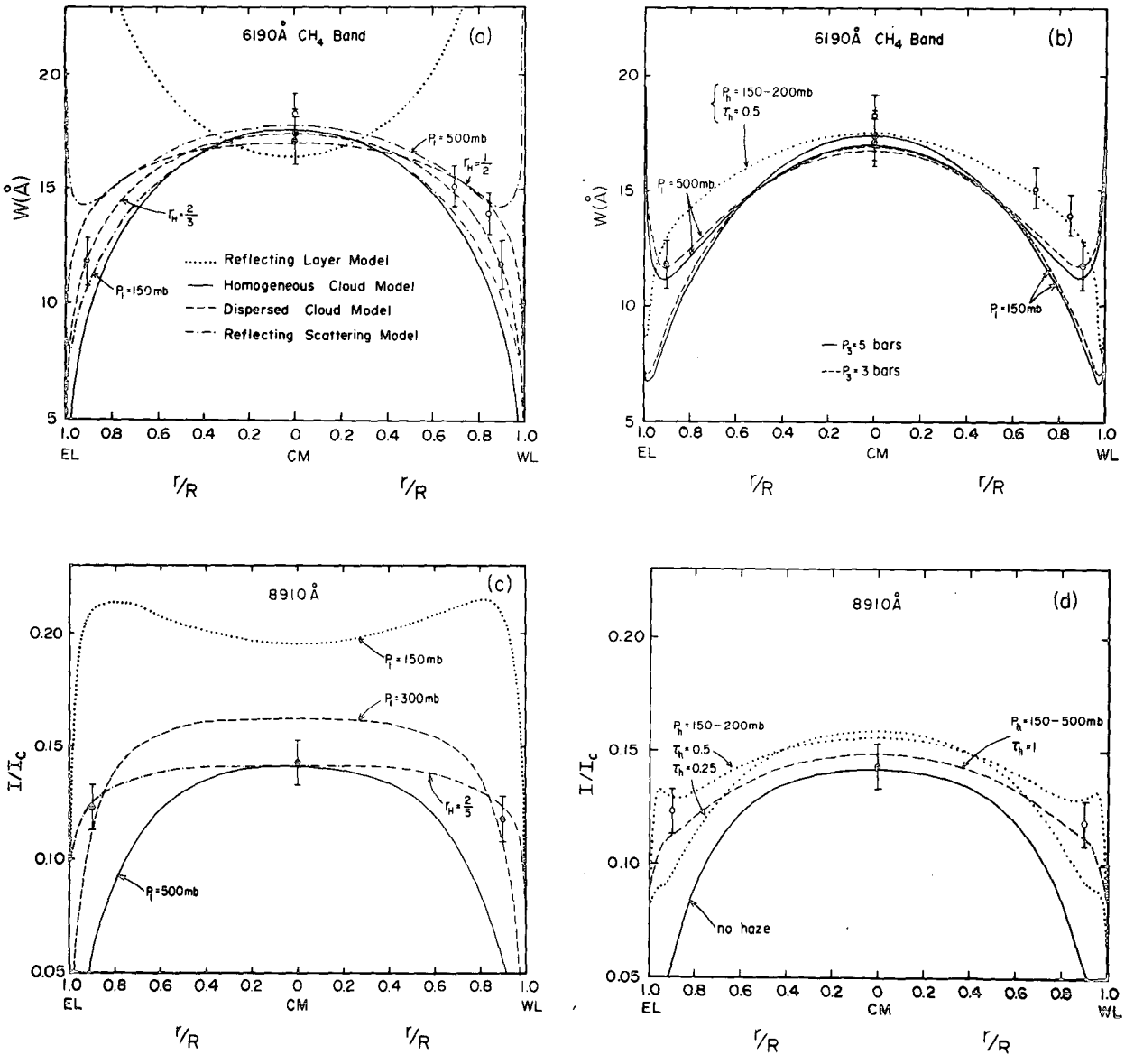

FIG. 14. CTLV of methane absorption. (a) and (b) are the CTLV of the equivalent width of 6190 Å CH_4 band. (a) shows how the simple models compare to observations of Woodman *et al.* (1979); model parameters are the same as for Fig. 10a. (b) shows the results for the TCM with P_2 = 700 mb and the methane abundance $[CH_4]/[H_2] = 1.8 \times 10^{-3}$ for all cases; the haze layer is added above the model with P_3 = 5 bars, P_1 = 500 mb. (c) and (d) are the limb-darkening relative to the continuum at 8910 Å. (c) shows that the CTLV depends substantially on the level of the upper cloud top; it also shows that a flat CTLV is obtained if the entire upper cloud (from 700 mb to 150 mb) is a dispersed cloud with scale height about half or less that of the gaseous atmosphere. (d) shows that a haze above the top cloud can also flatten the CTLV, making it similar to the observations; for this case P_2 = 700 and P_3 = 5 bars.

b. Planetary observations

Several observations of the equivalent widths of the ammonia bands are compared in Table 4. There is a substantial spread in the observed values; this may partly reflect real-time variability, which is particularly likely for an inhomogeneously mixed gas.

The observations are usually reported in terms of an ammonia abundance for the RLM or the [C]/[N] ratio obtained by comparison with a nearby methane band. Woodman *et al.* (1977) used their observations of the center of the disk and the RLM to obtain 34 ± 4 m-am from the 5510 Å band and 13.1 ± 0.7 m-am from the 6450 Å band, an inconsistency by a factor 2.6. Similar discrepancies are obtained from the other observations.

Woodman *et al.* (1977) compared the 5510 Å NH_3 band with the 5430 Å CH_4 band obtaining [C]/[N] = 7.5 ± 1.4 and they compared the 6450 Å NH_3 band with the 6190 Å CH_4 band obtaining [C]/[N] = 14.9 ± 1.6, in both cases under the assumption that $[CH_4]/[NH_3]$ = [C]/[N]. Owen (1978, private

TABLE 4. Measured equivalent widths of 6450 and 5510 Å ammonia bands.

Observers	W (Å) 6450 Å	W (Å) 5510 Å	Position on Jupiter	Date
Teifel (1969)	5.4 ± 2.4		ER at CM	April and May 1968
Avery *et al.* (1974)	3.3 ± 0.6		ER at CM	July 1972
Encrenaz *et al.* (1974)	8 ± 1		ER at CM	October 1973
Woodman *et al.* (1977)	7.2 ± 0.4	1.7 ± 0.2	ER at CM	November 1974 and
	4.7 ± 0.4	1.5 ± 0.4	¾ of full CM	January 1976
Owen (private communication)		2.1	ER at CM	January 1976
		1.2	NP at CM	
		1.1	SP at CM	
		2.1	GRS	
Woodman *et al.* (1979)	5.9 ± 0.7	1.4 ± 0.4	ER at CM	November 1976
	6.3 ± 0.7			
	4.7 ± 0.7	1.6 ± 0.4	NEB at CM	
	4.5 ± 0.7			
	3.3 ± 0.7	0.9 ± 0.4	NTrZ at CM	
	2.8 ± 0.7			
Lutz (1978)	11.3	2.1	ER at CM	February 1977

communication) obtained [C]/[N] = 6.6 ± 1.0 from the 5510 and 5430 Å bands. Lutz (1978) obtained [C]/[N] = 7.0 from these same bands, and 9.6 from the 6190 Å CH_4 band and the 6450 Å NH_3 band. Combes and Encrenaz (1979) obtained [C]/[N] = 19 (+13, −7) by comparing the $3\nu_3$ CH_4 band at 1.1 μm with the NH_3 band at 1.56 μm. The solar value of [C]/[N] is ~4.8 (Table 1).

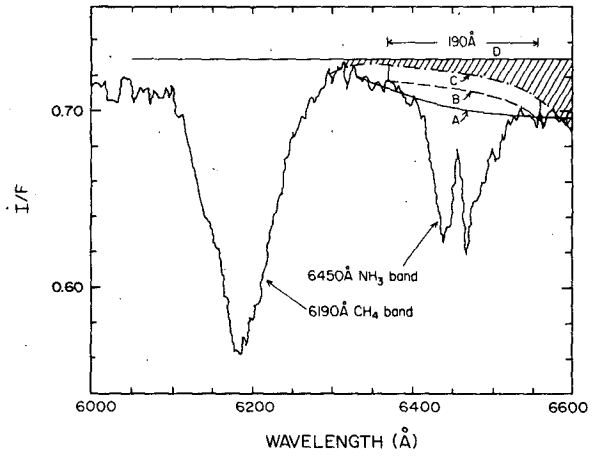

FIG. 15. Spectrum measured by Woodman *et al.* (1979) for the ER of Jupiter. Curve A (Cochran, private communication) is the continuum employed by Woodman *et al.* to obtain the value they reported for the equivalent width of the 6450 Å NH_3 band. The shaded area is the methane absorption in this region. Thus the appropriate continuum for this band has the shape of curve C, but its vertical location is uncertain. Curve B defines the minimum equivalent width for the bandwidth measured in the laboratory by Lutz (1979).

c. Atmospheric models

It is important that the observed and modeled equivalent widths be defined consistently, specifically with regard to the continuum level. We show below that if account is taken of the overlap of methane absorption with the 6450 Å ammonia band, the discrepancy in ammonia abundance between the 5510 and 6450 Å bands largely disappears.

Fig. 15 shows the 6190 Å CH_4 band and 6450 Å NH_3 band observed by Woodman *et al.* (1979). The solid sway-backed curve (A) is the continuum used by Woodman *et al.* in their determination of the equivalent width of the 6450 Å NH_3 band. It is difficult to choose the continuum for this band *a priori* because of methane absorption in the same region. But fortunately both the methane and ammonia absorptions are weak and thus essentially additive; also the methane absorption is continuous with an absorption coefficient which has been measured across the entire ammonia band (cf. Section 5). We can thus compute the amount of methane absorption in the region of the NH_3 band, using the methane abundance determined in Section 5. Any of the models which are consistent with both the weak and strong CH_4 absorptions yield the same result for the present purpose; we employed the TCM. The cross-hatched region in Fig. 15 shows the resulting methane absorption in the region of the ammonia band. The appropriate continuum for the NH_3 band is still uncertain, however, because the continuum used to compute the methane absorption, the straight line at $I/F = 0.73$, is some-

what arbitrary. Thus the dash-dot curve in Fig. 15 gives the appropriate shape for the NH_3 band continuum, but can be moved vertically. The smallest possible equivalent width is that defined by continuum B, which was chosen such that the width of the resulting ammonia band is the same as the spectral width (190 Å) to which the laboratory absorption parameters apply. However, this equivalent width is a lower limit, because 1) the ammonia absorption is probably not identically zero at the edges of this spectral interval, and 2) although both bands are weak, they are not strictly additive.

The lower limit for the 6450 Å NH_3 equivalent width in the spectrum of Woodman *et al.* (1979) for the ER is thus 8.4 Å, corresponding to continuum B in Fig. 15. The upper limit is more subjective; we use continuum C to define the width of the observational bar in Fig. 16. The definition of the continuum for the weaker bands in the 5000–6000 Å region is straightforward since there is no evidence of major overlap there.

Fig. 16 compares the observed ammonia equivalent widths with the RLM and TCM. Because both bands are weak there is little dependence on cloud model structure, although the TCM is in slightly better agreement with observations. There is only a small inconsistency between the abundances determined from the two bands. The ammonia abundance is specified in Fig. 16 as the ratio $[NH_3]/[H_2]$ in units of 1.9×10^{-4}, so that $n = 1$ corresponds to the currently accepted nitrogen abundance in the atmosphere of the sun (Table 1).

Fig. 16 also illustrates the sensitivity of the derived NH_3 abundance to nonuniform mixing of NH_3 gas. If NH_3 is assumed to be uniformly mixed, as is often the case for the rough interpretations accompanying reported observations, the value of n obtained is significantly smaller than that obtained when

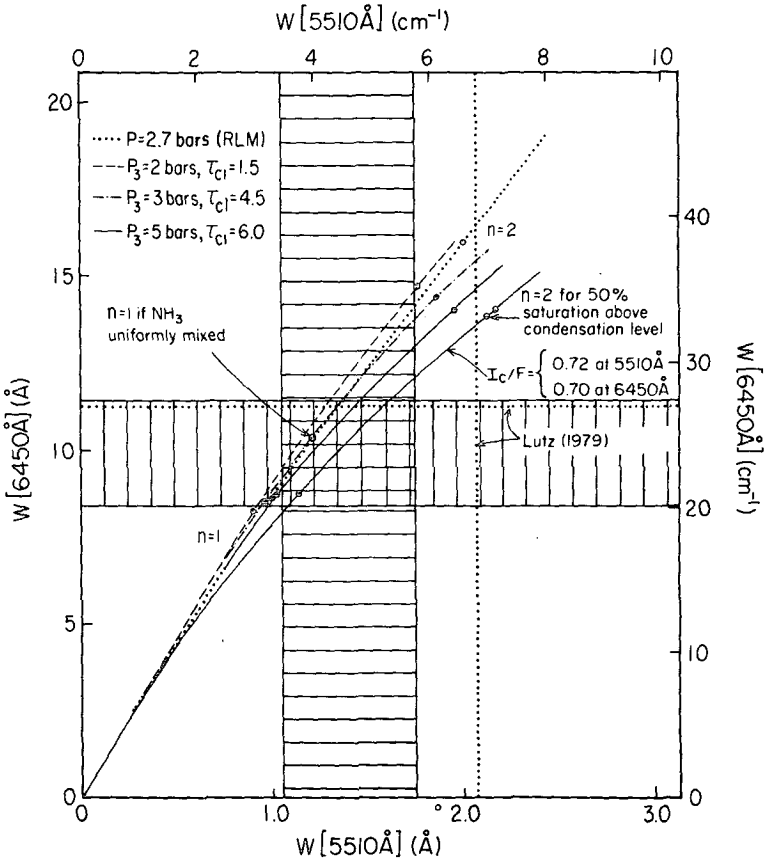

FIG. 16. Equivalent widths of 5510 and 6450 Å ammonia bands for the RLM and TCM. The observational bars are based on data of Woodman *et al.* (1979) with the limits of the 6450 Å bar defined by continuum levels B and C in Fig. 15. Recent observations of Lutz (1979) are also shown. For the TCM P_1 is 500 mb and P_2 varies with ammonia abundance from 630 mb for $n = 1$ (1.9×10^{-4} for $[NH_3]/[H_2]$) to 690 mb for $n = 2$. The sensitivity of the calculations to uncertainties of the absolute continuum reflectivity between the two bands is illustrated.

supersaturation is not permitted. On the other hand, once supersaturation is eliminated further reduction of the ammonia above the level of condensation has only a small effect on the equivalent widths. This is because, with the ammonia abundance limited to the saturation amount, already 80–90% of the absorption in the 5520 and 6450 Å bands occurs beneath the ammonia clouds. For the same reason, the derived ammonia abundance is relatively insensitive to the value of the cloud-top pressure P_1 or the properties of the haze above the top cloud layer.

The above results indicate that there is a region of ammonia condensation in the Jovian atmosphere; n would have to be $\lesssim 10^{-3}$ to avoid having condensation (cf. Fig. 2). The level of ammonia condensation coincides with the region in which extensive multiple scattering is required to explain CH_4 and H_2 absorptions (cf. Sections 4 and 5); the CH_4 and H_2 data also indicate the need for a clearer region beneath this cloud layer, and then a second reflecting layer at a depth of 3–5 bars. Thus, because of the location of the upper cloud layer and the proof that ammonia condensation occurs there, we can identify the upper cloud as ammonia. As a result of the temperature in this layer, we can also conclude that the ammonia particles are in a solid, presumably crystalline, form. Of course, it is possible that two cloud materials coexist in this region or that there is a significant amount of impurities in the ammonia particles. Therefore, in Section 7 we explicitly examine the consequences of possible absorption in the upper cloud region.

There is substantial variation in the observed ammonia equivalent widths, much of which probably represents real-time variability. Since most of the absorption in the 5510 and 6450 Å bands occurs beneath the ammonia cloud layer, the simplest interpretation would be a change in the transparency of that layer due to change in the cloud optical thickness, the extent of holes in the cloud or the amount of cloud particle absorption. It would be extremely valuable to have complete spectra with the quality of those of Woodman *et al.* (1979) obtained at several different times but with the same instrumentation. The ratio of such spectra could be subjected to the type of analysis described in Section 7 to obtain information on the time variation of cloud and haze properties.

We conclude from the existing data that the NH_3 abundance is $n = 1.5 \pm 0.5$, i.e., $[NH_3]/[H_2] = (2.8 \pm 1.0) \times 10^{-4}$. This value is the average for the region from $P \approx 1$ bar to $P \approx 3$–5 bars. If the second cloud deck is H_2O, the ammonia abundance in the region between the ammonia and water clouds may be reduced by solution in the water clouds. Thus the ammonia abundance in the bulk of the atmosphere may be somewhat larger than indicated by the above number.

7. Cloud-top region and haze structure

In the previous sections we focused on observations which probe the region of atmospheric pressures from a few hundred millibars to several bars. In this section we consider observations sensitive to the level of the cloud tops and the possible presence of aerosols at higher altitudes. Our objective is to verify that the structure in these upper levels does not substantially affect our earlier conclusions, as well as to obtain information on the atmospheric structure at the higher altitudes. We employ three techniques to probe this region: (i) variation of reflectivity as a function of the methane absorption coefficient, the larger absorption coefficients referring to higher levels; (ii) center-to-limb variation (CTLV) of reflectivity, the values close to the limb referring to higher levels; and (iii) variation of the reflectivity with wavelength in the ultraviolet, the shorter wavelengths referring to higher levels as a result of increased Rayleigh scattering and absorption.

We first examine the red spectra (including the near infrared) of Woodman *et al.* (1979) employing techniques (i) and (ii) in that order. We start with the reflectivity on the central meridian to minimize the effect of high-altitude haze and thus permit investigation of the altitude of the cloud tops and to minimize complications in the interpretation due to horizontal inhomogeneities. The CTLV of reflectivities in the red is then studied to place some constraints on the properties of the aerosols above the primary ammonia cloud region.

We next examine the blue spectra (including the near ultraviolet) of Woodman *et al.* (1979) employing techniques (ii) and (iii). We anticipate that the blue spectra will be useful for establishing properties of the high-altitude aerosols, aided by any constraints from the red region.

We pay particular attention in both spectral regions to variations between belt and zone regions on Jupiter, employing the observations by Woodman *et al.* (1979) of the NEB and NTrZ, which were relatively well-defined regions at the time of the observations. By examining the ratio of these spectra we anticipate that it may be possible to deduce how key cloud and aerosol parameters differ between the two regions, even though the spectra are basically very similar.

a. Red spectra

We first examine the reflectivity in the NTrZ as a function of the methane absorption coefficient to verify that we have appropriate TCM parameters for that region. As described in Sections 4–6, with the assumption that $\tilde{\omega}_{cl} = 1$ the model parameters τ_{cl}, R_3 and P_3 are determined from 1) the reflectivity in the continuum ($k \to 0$), 2) the hydrogen quadrupole line strength (equivalent to requiring the reflectivity

to fit at wavelengths of weak methane absorption, if the methane abundance is fixed), and 3) the reflectivity in a strong methane band (i.e., from a comparison such as in Fig. 10). The solid curve in Fig. 17 shows that the TCM parameters estimated for the NTrZ in this way provide good agreement with the observed reflectivity through the complete spectrum of methane absorption coefficients.

Fig. 17 also illustrates that even if all of the continuum absorption is placed in the ammonia cloud layer ($R_3 = 1$), the TCM fits the observations well. In the extreme model shown $P_3 = 2.5$ bars, $\tau_{cl} = 6.5$ and $\tilde{\omega}_{cl} = 0.989$. A continuous spectrum of TCM's fits the methane absorption spectrum corresponding to R_3 varying from 0.7 to 1. As R_3 increases through this range P_3 decreases from 4–5 bars to ~2.5 bars.

The ratio of the NTrZ and NEB reflectivities, which we abbreviate as NTrZ/NEB, has features at wavelengths of methane and ammonia absorption bands (Fig. 18). These features must be related to differences in cloud structure between the NTrZ and NEB, and they provide the basis for a technique to analyze those differences. Fig. 19 shows the ratio of reflectivities plotted as a function of methane absorption coefficient. The NTrZ is 6–8% brighter than the NEB in the continuum, and for small to intermediate values of k NTrZ/NEB increases with increasing k. However, for large k the ratio decreases sharply.

In order to analyze the information in NTrZ/NEB we calculate the theoretical dependence of the ratio on cloud-model parameters. In the computations illustrated in Fig. 19 the haze properties are kept fixed (with $\tau_h = 0.5$, $\tilde{\omega}_h = 1$ and the particles uniformly distributed through the region 150–200 mb), but we later examine the effect of the haze. We first investigate whether the observed NTrZ/NEB can be reproduced by changing only one model parameter. The magnitude of the parameter change is chosen to be that which yields the observed reflectivity in the continuum. Thus changing τ_{cl} from 6 in the NTrZ to 1.5 in the NEB gives the correct continuum reflectivity, but NTrZ/NEB increases far too rapidly with increasing k (Fig. 19a). On the other hand, if the lower continuum reflectivity in the NEB is achieved by adding absorption in either the ammonia cloud region (by decreasing $\tilde{\omega}_{cl}$) or at the lower cloud (by decreasing R_3) the computed reflectivity ratio decreases monotonically with increasing k (Fig. 19a). Changes in other cloud parameters, such as P_1 alone, cannot even yield the observed continuum reflectivity in the NEB.

The results for one-parameter changes suggest as the next step in complexity decreasing τ_{cl} in the NEB, while at the same time decreasing either R_3 or $\tilde{\omega}_{cl}$. The curves in Fig. 19b which are not labeled with P_1 values are the case when just τ_{cl} and $\tilde{\omega}_{cl}$ are changed; a satisfactory fit to the observations

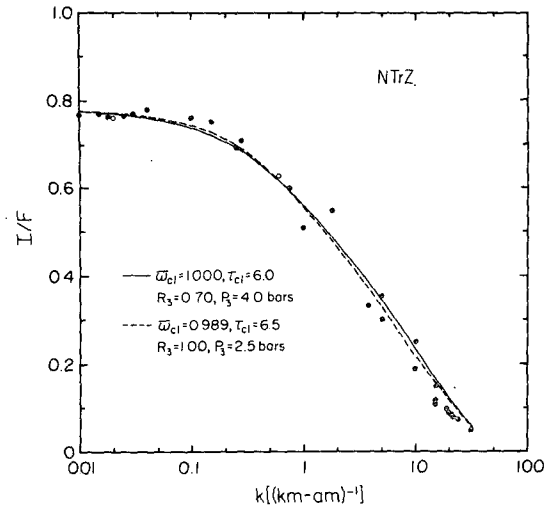

FIG. 17. Reflectivity of NTrZ in the red spectra of Woodman *et al.* (1979) as a function of the methane absorption coefficient of Giver *et al.* (1978); solid dots are points from 6750 Å–1 μm wavelength region, while open circles are from 6000–6750 Å. The model calculations employ the TCM with $P_1 = 500$ mb, $P_2 = 630$ mb and a conservatively scattering haze uniformly distributed between 150 and 200 mb with $\tau_h = 0.5$.

is still not achieved. Changing τ_{cl} and R_3 simultaneously (Fig. 19d) did not produce a better fit, a result which could be anticipated from the flat ratio of reflectivities at large k when R_3 alone is changed.

The obvious cloud-parameter change capable of producing the rapid decrease of NTrZ/NEB at large k is to have the cloud top higher in the belt (P_1 smaller). This is illustrated in Fig. 19b which includes three cases with higher cloud tops in the belt. There may in reality be several differences between the NEB and the NTrZ, but we have not found any straightforward way to reproduce the rapid falloff at large k except with a smaller P_1 over the NEB. However, there is additional scattering material above the P_1 level; this also seems to be distributed differently over the NEB than over the NTrZ, in a way which is discussed in the following subsection. The scattering material in this "haze" region may include thin "cirrus" clouds (i.e., $\tau \sim 1$–2) and localized clouds of greater optical thickness.

We also investigate the sensitivity of NTrZ/NEB to the location of the continuum absorption. The extreme case $R_3 = 1$, in which all of the absorption occurs in the upper cloud, is shown in Fig. 19c. The observed behavior of NTrZ/NEB as a function of k can be obtained in this case by having both τ_{cl} and $\tilde{\omega}_{cl}$ smaller in the belt than in the zone. Again, however it is also necessary for P_1 to be smaller in the belt.

The other extreme case, with $\tilde{\omega}_{cl} = 1$ in both NTrZ and NEB so that all absorption occurs at the lower cloud, is shown in Fig. 19d. This also has the basic features in the observations if P_1 is smaller

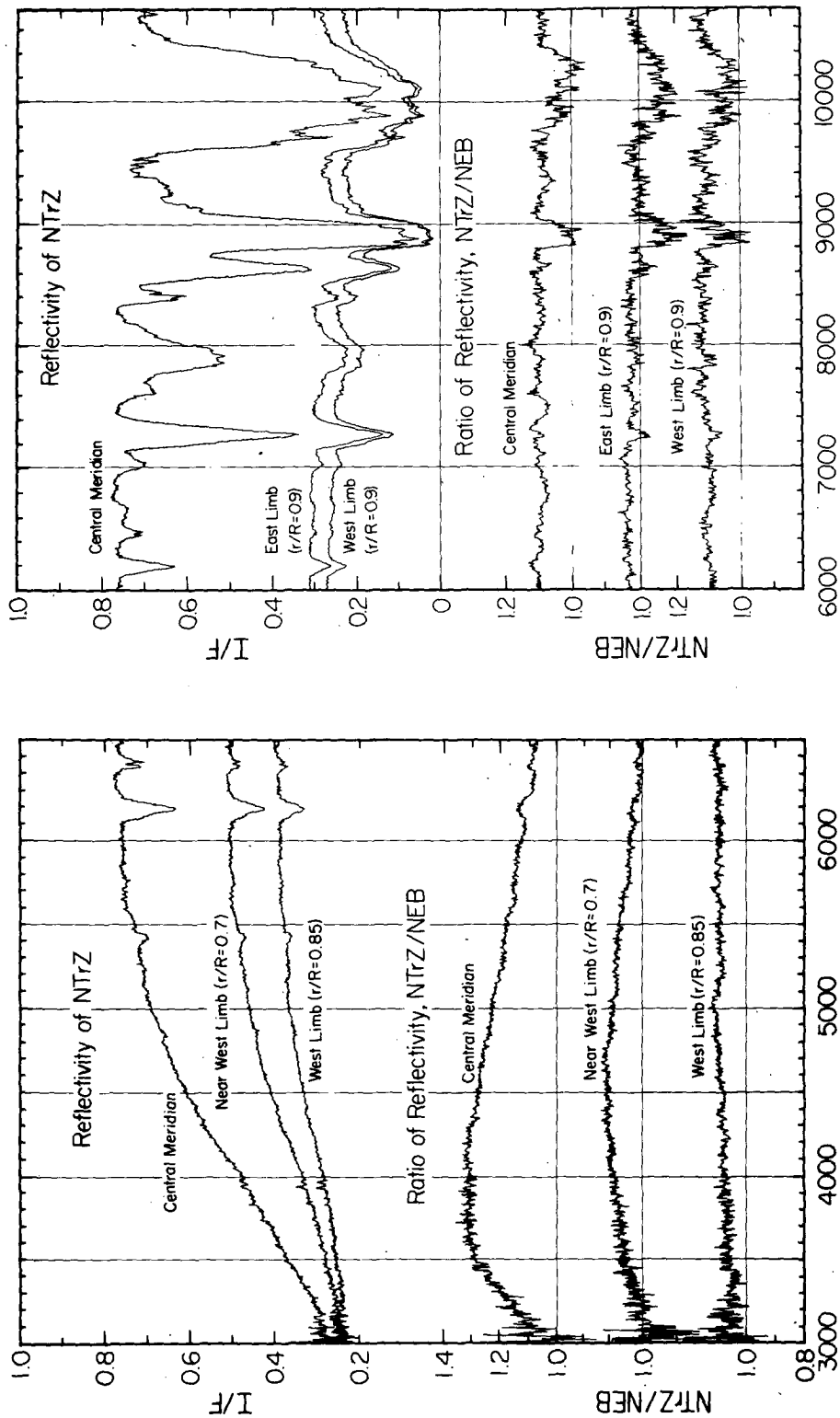

FIG. 18. Spectra of the NTrZ and the ratio of the NTrZ and NEB observed by Woodman *et al.* (1979).

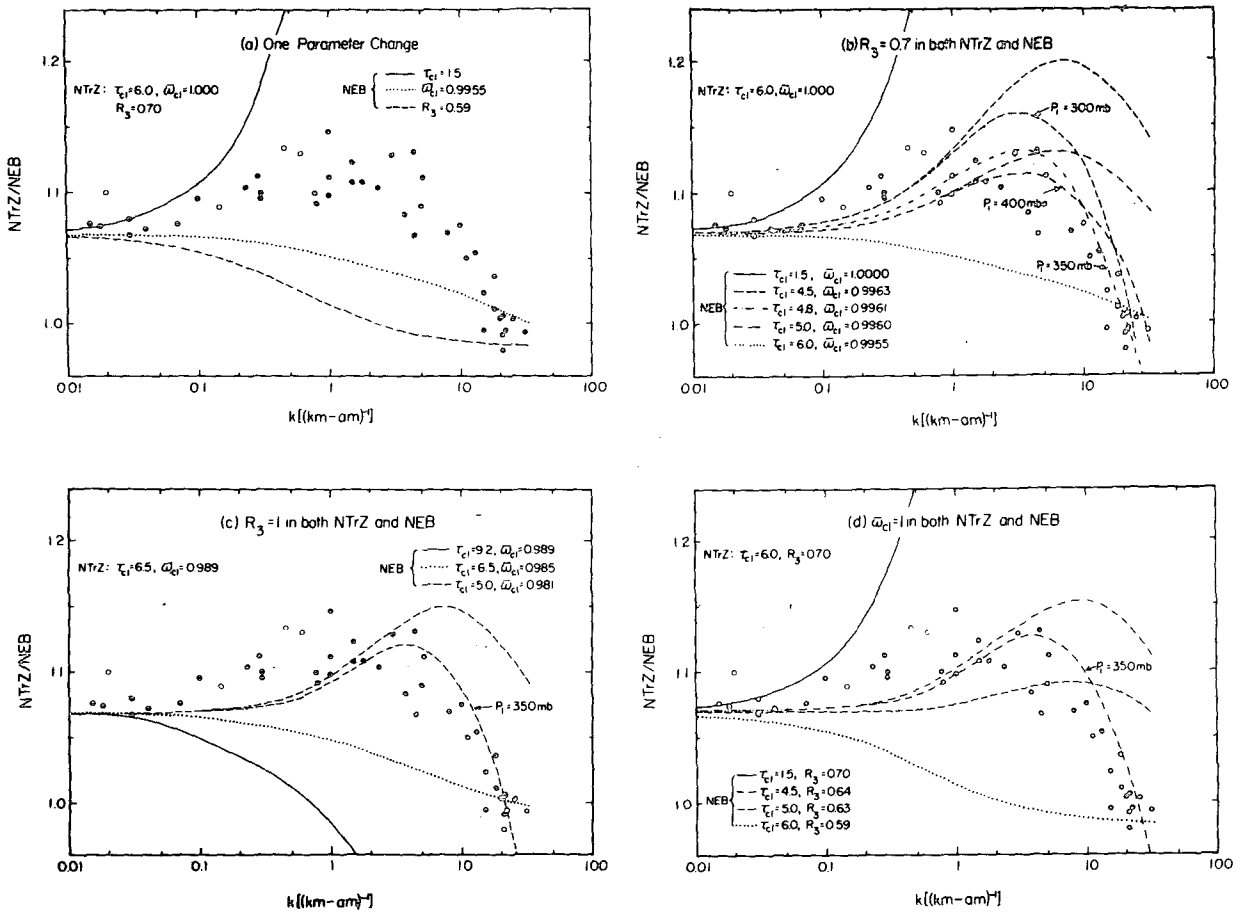

FIG. 19. Ratio of intensity NTrZ/NEB on the central meridian as a function of methane absorption coefficient k. Values of k are taken from Giver (1978) at wavelengths 6000–10 000 Å and the corresponding values of NTrZ/NEB from Woodman *et al.* (1979). The theoretical curves are obtained by making computations for the NTrZ with a given set of model parameters and then changing selected parameters for the NEB calculations. All models have a haze layer at 150–200 mb with $\tau_h = 0.5$ and $\tilde{\omega}_h = 1$, and a cloud bottom at $P_2 = 630$ mb. The top of the upper cloud is at 500 mb unless indicated otherwise. P_3 is 4 bars in parts (a), (b) and (d), and 2.5 bars in (c).

in the NEB than in the NTrZ. The fit to observations at intermediate values of k can be improved by allowing a small amount of absorption to occur in the upper cloud region rather than at R_3, at least in the belt, as illustrated in Fig. 19b. However, we do not believe that much significance can be attached to such fine tuning.

The information on cloud structure obtained from the ratio of reflectivities NTrZ/NEB can be summarized as follows:

1) The only cloud-model parameter (for the TCM constrained as described in Sections 4–6) capable of producing the observed rapid decrease of NTrZ/NEB at large k is P_1, implying that the cloud top is at a level of smaller pressures in the NEB than in the NTrZ.

2) There is a continuous range of models in which R_3, τ_{cl} and $\tilde{\omega}_{cl}$ can be adjusted to give the observed behavior of NTrZ/NEB in the continuum and at small values of k. The uncertainty in R_3, which may be anywhere in the range ~0.7–1.0, implies a corresponding range of possible values for P_3 from ~6 bars to ~2.5 bars. There is weak evidence in the observations against either extreme case, which would suggest $P_3 \sim 3$–5 bars.

We next examine the Woodman *et al.* (1979) observations of the ratio of the reflectivity near the west limb to the reflectivity at the central meridian, which we abbreviate as WL/CM. These data are primarily useful for characterizing the high-level haze whose existence is indicated by both the CTLV of the reflectivity in the methane bands (Section 6) and in the ultraviolet. Two basic parameters are needed to define the haze, τ_h and $\tilde{\omega}_h$, in addition to the vertical distribution. We cannot determine all of these from the WL/CM in the red, but we can put some limits on τ_h and $\tilde{\omega}_h$ for any assumed vertical distribution of haze. We will then employ these constraints when we analyze the blue spectra.

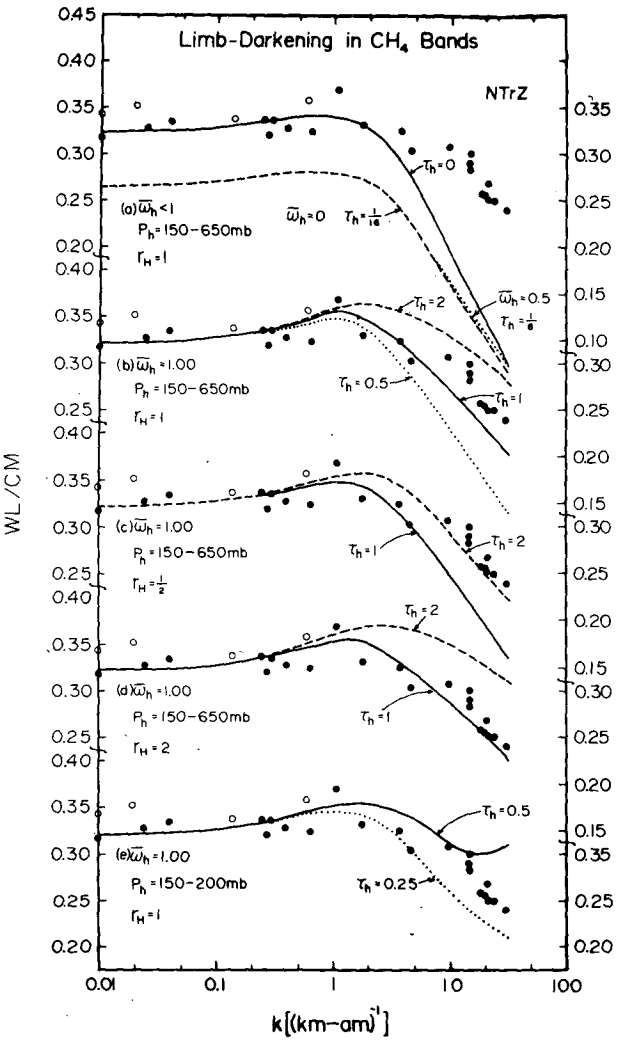

FIG. 20. Ratio of the intensities near the west limb ($r/R \approx 0.9$) and at the central meridian in the NTrZ as a function of methane absorption coefficient in the range 6000–10 000 Å. Theoretical results in (a) are for no haze ($\tau_h = 0$), for Axel dust ($\tilde{\omega}_h = 0$) with $\tau_h = 1/16$, and for $\tilde{\omega}_h = 0.5$, $\tau_h = 1/8$. Theoretical results in (b)–(e) are all for scattering aerosols ($\tilde{\omega}_h = 1$), but different vertical distributions; r_H is the ratio of haze scale height to gas scale height. In all cases $P_1 = 500$ mb, $P_2 = 650$ mb, $P_3 = 4$ bars and $\tilde{\omega}_{cl} = 1$. In (b)–(e) $R_3 = 0.7$ and $\tau_{cl} + \tau_h = 6.5$. In (a) $R_3 = 0.7$ and $\tau_{cl} = 6.5$ for the case of no haze, but $\tau_{cl} = 8.5$ and $R_3 = 0.86$ for the case of haze with $\tilde{\omega}_h = 0$ or 0.5.

Fig. 20 contains the observations of WL/CM in the red in the NTrZ, plotted as a function of k. The model comparisons include the extreme cases of Axel dust ($\tilde{\omega} = 0$) and a conservatively scattering haze ($\tilde{\omega} = 1$). Axel dust is inconsistent with the observations, as shown in Fig. 20a; it produces a much larger limb-darkening than observed at large k. Scattering aerosols, on the other hand, are consistent with the observations for some optical thickness which depends upon the assumed vertical distribution (Figs. 20b–20e). The observed WL/CM is similar for the NEB (not illustrated), and thus basically similar constraints on $\tilde{\omega}$ and τ are obtained for that region.

Several caveats must be attached to interpretation of the WL/CM observations: knowledge of pointing direction is uncertain by about 1 arc second (Cochran, private communication), the observed results are sensitive to atmospheric seeing conditions and spreading due to the finite aperture size, and the computations depend on the assumed phase function and possible horizontal atmospheric inhomogeneities. Therefore, we draw only very gross conclusions: 1) in the red the high-altitude haze is considerably closer to $\tilde{\omega} = 1$ than to $\tilde{\omega} = 0.5$ and 2) for a specified vertical distribution of haze and specified P_1, an estimate of the haze optical thickness can be obtained which should be accurate within about a factor of 2 (Fig. 20).

b. Blue spectra

The decreasing reflectivity of Jupiter from the visible to the ultraviolet (Figs. 4 and 17) was the basis for Axel's (1972) suggestion of absorbing aerosols in the upper atmosphere of Jupiter. Axel assumed that the particles were smaller than the wavelength in the ultraviolet and that their optical properties were thus approximated by $\tilde{\omega} = 0$ and $\tau \propto \lambda^{-1}$. He believed that the spectral reflectivity of Jupiter was consistent with these properties.

We begin analysis of the blue spectra of Woodman *et al.* (1979) by considering the extreme case of Axel dust and the opposite extreme which we term "scattering aerosols". The scattering aerosols are assumed to be larger than the wavelength so that their optical thickness can be approximated as independent of wavelength in the blue and red spectra; it is assumed that the ultraviolet absorption is due to deviations of $\tilde{\omega}_h$ from unity.

The requirement to reproduce the observed blue spectra specifies $\tau_h(\lambda)$ in the case of Axel dust or $\tilde{\omega}_h(\lambda)$ in the case of scattering aerosols provided that the vertical distribution of the haze is known. The upper part of Fig. 21 shows the optical thickness of Axel dust needed to produce the observed reflectivity of the NTrZ on the CM, for several assumed vertical distributions of this haze layer. The lower part of the figure shows the single-scattering albedo required for scattering aerosols. For the NEB the results are qualitatively similar, with $\tau_h(\lambda)$ for Axel dust somewhat larger or $\tilde{\omega}_h(\lambda)$ for scattering aerosols smaller than in the NTrZ.

The required $\tau_h(\lambda)$ for Axel dust is self-contradictory with the basic assumptions of that model, which require $\tau_h \propto \lambda^{-1}$. It was shown above that Axel dust is also inconsistent with the observed CTLV in the red spectra. Because the discrepancies with observations are so large, it can be concluded

that Axel dust or a similar model (i.e., $\tilde{\omega} \ll 1$) is not responsible for the continuum absorption on Jupiter.

The required $\tilde{\omega}_h(\lambda)$ for scattering aerosols is physically plausible and consistent with the basic assumption of large particle size. The expression

$$\tilde{\omega}_h(\lambda) = \frac{1}{1 + \tau_a/\tau_s} = \frac{1}{1 + 10^{-6.4\lambda+1.7}} \qquad (14)$$

fits the observed reflectivity of the NTrZ CM within a few percent for $3000 < \lambda < 6350$ Å, for the case of a uniform distribution of scatterers with $\tau_h = 1.5$ between 150 and 650 mb. A different vertical distribution for the scatterers modifies $\tilde{\omega}_h$ as shown in Fig. 21, but would have little affect on the relative wavelength dependence of the absorption optical thickness τ_a. Similarly, $\tilde{\omega}_h$ is larger than given by (14) if the particles are large enough to produce diffraction, but this has little affect on the relative wavelength dependence of τ_a.

The single-scattering albedo $\tilde{\omega}_h(\lambda)$ can be converted to the absorption coefficient of the material composing the aerosols, if an aerosol size is assumed. Table 5 shows the results of such a computation for the approximation of spherical particles. Particularly since the absorption may be due to an impurity (minor constituent) in the scatterers, the absolute value of k is less significant than the relative wavelength dependence. However, the latter may be useful for helping to identify the composition of the absorber. For example, hydrazine (Strobel, 1973) is not consistent with the $k(\lambda)$ in Table 5 but some hydrocarbons (Scattergood and Owen, 1977) have approximately the required relative wavelength dependence for k. A careful comparison with the absorption coefficients of these and other candidate constituents, e.g., sulfur, phosphorus, NH_4SH, HgS and PO_3 (Prinn and Owen, 1976), would perhaps be worthwhile.

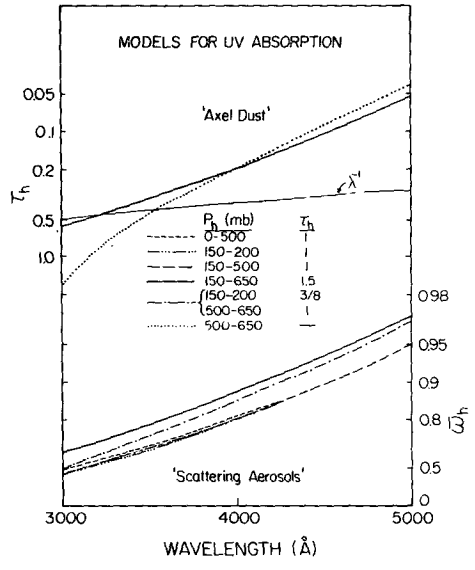

FIG. 21. Optical thickness of Axel dust ($\tilde{\omega}_h = 0$) and single-scattering albedo of scattering aerosols [$\tau_h(\lambda)$ = constant] required to yield the reflectivity observed by Woodman *et al.* (1979) for the central meridian of the NTrZ. Results depend on the vertical distribution of the haze as indicated. In all cases the cloud structure was specified as $P_1 = 500$ mb, $P_2 = 650$ mb, $P_3 = 4$ bars, $\tilde{\omega}_{cl} = 1$ and τ_{cl} such that $\tau_{cl} + \tau_h = 6.5$.

TABLE 5. Aerosol absorption coefficient k (cm^{-1}) required to produce the observed reflectivity in the NTrZ. $k = 4\pi n_i/\lambda$ where n_i is the imaginary part of the refractive index. Aerosols are approximated as spheres uniformly distributed between 150 and 650 mb.

Aerosol radius (μm)	Wavelength (Å)			
	3000	4000	5000	6000
0.3	30000	6000	1500	300
1.0	9000	1500	300	60
10.0	1500	200	30	10

The UV absorption must occur in both the ammonia cloud region and in the haze region, as demonstrated by comparison of several extreme models with the observed CTLV in the blue spectra (Fig. 22). If there were no absorption in the haze region, the WL/CM reflectivity ratio would be significantly larger than observed. This is shown by the case "no aerosols above 500 mb" in Fig. 22; addition of conservatively scattering aerosols in this region would make the discrepancy with observations larger. On the other hand, if all the absorption is placed in the 150–200 mb region, or even 150–500 mb, the WL/CM ratio has more limb-darkening than observed. Thus a substantial amount of absorption must occur in the main cloud region at depths $\gtrsim$500 mb. Since ammonia does not provide the required absorption, this region must include some constituent other than ammonia.

Figs. 22 and 23 also suggest that the haze is concentrated higher in the atmosphere in the NTrZ than it is in the NEB. In Fig. 23 we have plotted the ratio of reflectivities, NEB/NTrZ. This graph makes clear the difference in behavior of the belt and zone toward the shortest wavelengths. An increase of NEB/NTrZ toward 3000 Å can be obtained in the model if the scattering aerosols are

Finally, we explore the vertical distribution of the aerosols and the UV absorption. In doing so we describe the interval ~400–650 mb as the ammonia cloud region and the less optically dense interval ~150–400 mb as the haze region. It should be noted, however, that the haze region may include ammonia "cirrus" clouds ($\tau \sim 1$–2) and localized thicker clouds, and it will be shown that the ammonia cloud region includes material other than ammonia to provide required absorption.

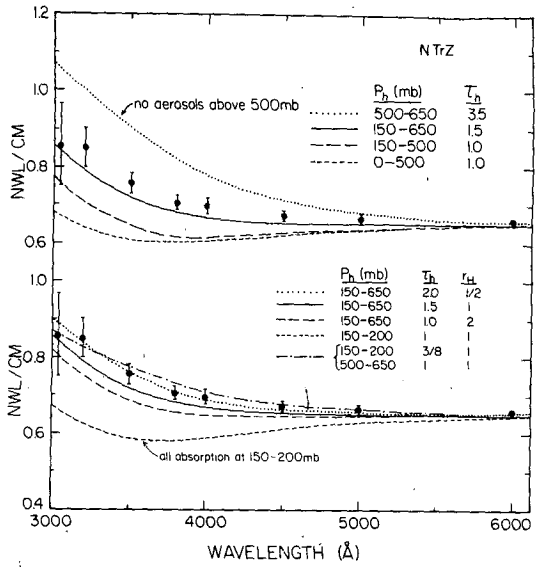

FIG. 22. Limb-darkening in the blue spectra of NTrZ. The near west limb (NWL) position is at $r/R = 0.70$. Observations are by Woodman *et al.* (1979). Computations are for different vertical distributions of scattering aerosols with the $\tilde{\omega}_h(\lambda)$ (Fig. 21) required to give the observed intensity at the central meridian (CM). In all models the clouds were specified by $P_1 = 500$ mb, $P_2 = 650$ mb, $P_3 = 4$ bars, $\tilde{\omega}_{cl} = 1$, $R_3 = 0.7$ and τ_{cl} such that $\tau_{cl} + \tau_h = 6.5$.

lower in the belt than in the zone, so that there is more Rayleigh scattering over the belt. If the haze is uniformly distributed between 150 and 650 mb in the NTrZ, it must be located mainly within the ammonia cloud region in the NEB to yield the observed increase of NEB/NTrZ toward 3000 Å. The same qualitative conclusions are obtained for other assumed aerosol distributions in the NTrZ. The resulting aerosol distributions in the NEB have a relatively small optical depth in the region 150–400 mb.

The four primary conclusions indicated by the calculations in this section are as follows:

1) The aerosols above the ammonia cloud region are scattering aerosols (size $\gtrsim\lambda$, $\tilde{\omega} \approx 1$), not Axel dust (size $<\lambda$, $\tilde{\omega} \sim 0$); their decreasing affect on the Jovian albedo with increasing wavelength is due to an increasing $\tilde{\omega}_h$ rather than a decreasing τ_h, and thus it reflects a changing bulk absorption coefficient of the material composing the aerosols.

2) The UV absorption occurs in both the "haze" region (i.e., between 150 mb and 400–500 mb) and the denser "cloud" region just below.

3) The vertical distribution of the scatterers in the "haze" region is weighted toward higher altitudes in the NTrZ than in the NEB.

4) Top of the dense lower "cloud" layer is higher in the NEB than in the NTrZ.

These conclusions need to be carefully qualified. For example, the definition of cloud top is rather arbitrary. It is more rigorous to define the regions in terms of their optical density, as we do in the discussion in Section 9, since the "haze" region may include thin "cirrus" and thicker localized clouds, and the "cloud" region must include an absorbing material in addition to ammonia.

8. Miscellaneous checks

In this section we examine the compatibility of two specific three-cloud models proposed for Jupiter with the observations of Woodman *et al.* (1979), the effect of uncertainty in the hydrogen quadrupole line strength on information inferred from the analyses in earlier sections of the paper, the consistency of our model with observed belt/zone differences in hydrogen quadrupole line strength, and the sensitivity of our conclusions to the assumed aerosol and cloud particle phase functions. Earlier in the paper we included other checks on our analysis, for example, by examining the equivalent width and line width of methane absorption in the $3\nu_3$ region (Section 6).

a. Three-cloud models

In the two-cloud model (TCM) which we derived, the second cloud layer is at a depth (3–5 bars) significantly greater than in other TCM's for Jupiter. A prime aspect of this conclusion is that it apparently excludes the thick NH_4SH cloud layer

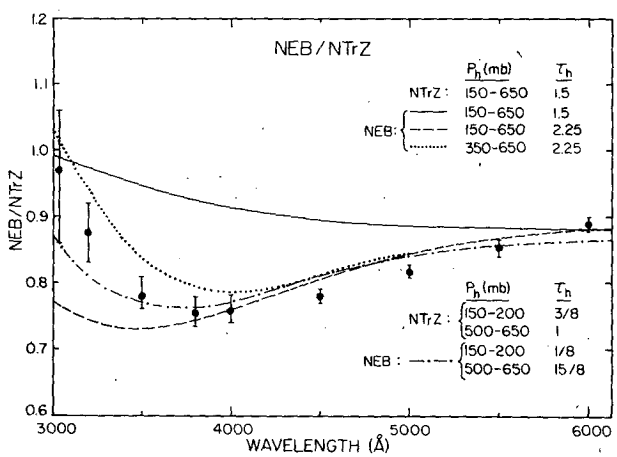

FIG. 23. Reflectivity ratio NEB/NTrZ on the central meridian for the 3000–6000 Å. Observations are by Woodman *et al.* (1979). Models show the effect of the haze vertical distribution for the case in which $\tilde{\omega}_h(\lambda)$ is the same for the NTrZ and NEB; $\tilde{\omega}_h(\lambda)$ is derived from the NTrZ reflectivity as shown in Fig. 21. The haze is uniformly distributed in the indicated intervals with the optical depths shown. The results for a case in which the haze was distributed with scale height ratio $r_H = 1/4$ and $\tau_h = 2.25$ in the NEB and $r_H = 1$ and $\tau_h = 1.5$ in the NTrZ ($P_h = 150$–650 mb in both regions) were indistinguishable from the dash-dot curve. Cloud model parameters in all cases were $P_2 = 650$ mb, $P_3 = 4$ bars, $R_3 = 0.7$ for both the NTrZ and NEB, $P_1 = 500$ mb, $\tilde{\omega}_{cl} = 1$, $\tau_{cl} + \tau_h = 6.5$ for the NTrZ, and $P_1 = 350$ mb, $\tilde{\omega}_{cl} = 0.99$ and $\tau_{cl} + \tau_h = 5.3$ for the NEB.

predicted by Weidenschilling and Lewis (1973) for the 1.5–2.0 bar region.

The vertical resolution of the remote sensing technique we have employed is very coarse for depths ≥ 1 bar. Thus the existence of an NH_4SH cloud may be consistent with the observations if the cloud layer is sufficiently transparent. To quantitatively investigate that possibility we made computations for a three-cloud model with the upper cloud between 500 and 630 mb, the second cloud between 1.4 and 1.6 bars, and the top of the dense lowest cloud at 4 bars. The location of the bottom of the second cloud is based on the NH_4SH abundance predicted by Weidenschilling and Lewis (1973) and the temperature profile of Orton (1977). We first take the optical thicknesses of the two upper clouds as being equal and assume conservative scattering in both layers. This requires $\tau_1 = \tau_2 = 3.5$ in order to yield the observed hydrogen quadrupole equivalent width. Fig. 24a shows that this model is not quite consistent with both strong and weak methane bands, since it yields an abundance $n = 1.7$ for the strong band and $n = 2.3$ for the weak band. If the NH_4SH cloud is taken as optically thicker than the NH_3 cloud, as indicated by the thermochemical equilibrium model, the result becomes considerably worse. However, consistency with the observations can be achieved by making the NH_4SH cloud optically thin. If the continuum absorption is placed in the NH_4SH cloud layer rather than in the lowest cloud, the extreme transparency requirement on the NH_4SH layer is partially alleviated. The required transparency may be obtained either by extensive holes in the clouds, or by a uniformly thin cloud deck.

We also investigated the three-cloud model of Terrile and Taylor (Terrile and Westphal, 1977; Terrile, Taylor and Beer, 1978). Based on observations at 5 μm they find evidence for cloud layers at temperatures <190, ~230 and ~300 K. Fig. 24b indicates that we can readily achieve consistency with their three-cloud model by choosing appropriate thicknesses for the upper two clouds.

The evidence for three emission temperatures at 5 μm does not support the three-cloud model of Weidenschilling and Lewis (1973). The ~230 K temperature of the second layer is too hot for NH_4SH clouds. On the contrary, the 5 μm observations are in agreement with our analysis which indicates a relatively transparent atmosphere between ~1 and ~3–5 bars. The temperatures 230 and 300 K correspond to $P \approx 2.5$ and 6 bars, based on the temperature profile of Orton (1977). Assuming that there are clouds at these two levels, we would expect our TCM to yield an intermediate pressure for the lower surface in order to provide an equivalent optical path for the H_2 4-0 line. Thus our result $P_3 \approx 3$–5 bars is in good agreement with the 5 μm observations.

One significant difference between our TCM and the conclusions of Terrile and Westphal (1977) is that we find clouds in the ammonia cloud region ($P < 1$ bar) over both the NTrZ and NEB, while Terrile concludes that they only exist over the zones.

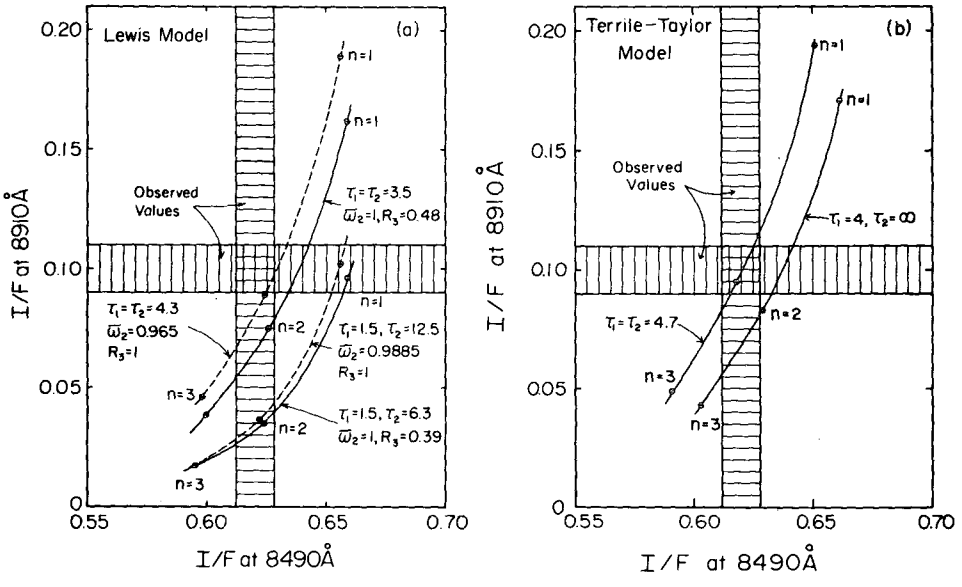

FIG. 24. Reflectivity at 8490 and 8910 Å. Observations are by Woodman *et al.* (1979). Calculations are for two three-cloud models. (a) is for the upper three clouds of Weidenschilling and Lewis (1973) assuming the temperature profile of Orton (1977), thus the clouds are at 500–630 mb, 1.4–1.6 bars and 4 bars. For (b) the cloud levels are 500–630 mb, 2.5–3.0 bars and 6 bars, the latter two cloud levels being based on the 5 μm temperatures of Terrile *et al.* (1978) and the temperature profile of Orton (1977).

Although the visual appearance of the white zones and darker belts is qualitatively suggestive of Terrile's model, it is not possible to reconcile the reflection spectra of solar radiation with the absence of the upper cloud layer over the belts. Our results do suggest that the cloud layer above the 1-bar level is more transparent over the NEB than over the NTrZ, which may be due to a smaller optical thickness or a greater area of holes in the upper cloud layer of the belt. Of course the cloud opacities may be much different at 5 μm than in the visible, particularly if the cloud particle size is <5 μm.

b. Hydrogen quadrupole line strength

The hydrogen quadrupole line strength $S_{4,1}(297\ \text{K}) = 0.92 \times 10^{-4}$ was employed in most of our computations, based on laboratory measurements of Bergstralh *et al.* (1978) and Trauger *et al.* (1978). However, theoretical calculations (Poll and Wolniewicz, 1978) yield a value almost twice as large (cf. Section 4). If it turns out that this theoretical value is correct, the value which we obtained for the pressure at the lower cloud (P_3) and the abundances of CH_4 and NH_3 relative to H_2 must be modified. P_3 would be reduced by almost a factor of 2, to the range 1.5–3 bars. The abundances of CH_4 and NH_3, which are determined most reliably by the weak bands, would be increased by almost a factor of 2. Other more minor adjustments in the model would also be necessary; for example, P_1 would need to be somewhat smaller or the haze above the ammonia cloud would need to be thicker to prevent the strong methane bands from being deeper than observed.

The H_2 3-0 $S(1)$ line provides a useful check on the 4-0 line. The results for the 3-0 line (Fig. 8) suggest that the laboratory values for the 4-0 line strength should not be increased by more than 25–50%. However, because the hydrogen lines serve as a barometer for determining pressure levels and relative gaseous abundances, it is important that the discrepancy between the laboratory and theoretical values of the 4-0 line strength be fully resolved.

c. Belt/zone differences in H_2 equivalent widths.

Observations of Jupiter have revealed systematic differences in H_2 4-0 equivalent width (EW) between the belts and zones (Table 3). Cochran *et al.* (1976) found the EW to be about 12% larger in the NEB than in the STrZ and Carleton and Traub (1974) found the EW about 6% larger in the NEB than in the SEZ. We computed this EW for our TCM with parameters obtained earlier ($P_1 = 350$ mb and $\tau_{\text{cl}} \approx 5$ for the NEB, $P_1 = 500$ mb and $\tau_{\text{cl}} \approx 6$ for the NTrZ). The result obtained was 6% larger for the NEB. A larger difference between the belt and zone could be obtained by making the upper cloud relatively more transparent in the belt, i.e., τ_{cl} smaller, or conversely, making τ_{cl} larger in the zone.

This agreement in the nature of the belt/zone difference for the observations and model can be understood from Fig. 19, since the H_2 4-0 line is analogous to weak methane absorption. The larger EW for the belt occurs (in the model, at least) because the ammonia cloud region is slightly more transparent in the belt. The difference in EW for the two regions would be much larger than observed if there were no ammonia cloud layer over the belt.

d. Cloud particle phase function

In most of our computations we employed the Kawabata-Hansen phase function (Fig. 3) for the cloud particles and haze particles. In order to verify that our basic conclusions are independent of the phase function, we repeated several computations with two different phase functions: (i) isotropic scattering, and (ii) a two-term Henyey-Greenstein phase function with anisotropy parameters $\langle\cos\alpha\rangle$ of 0.80 and 0.65 with 94% weight to the former, which are the parameters obtained by Tomasko *et al.* (1978) from analysis of Pioneer 10 limb-darkening observations. Isotropic scattering provides an extreme simplified case, while the Henyey-Greenstein case serves to test the effect of a backscattering lobe on the phase function.

Computations for the H_2 4-0 line were made with these phase functions. It was found that $\tau_{\text{cl}} = 2.4$ for isotropic scattering and $\tau_{\text{cl}} = 5.2$ for the Henyey-Greenstein phase function were required to yield an equivalent width of 8 mÅ.[4] $\tau_{\text{cl}} = 6$ is needed for the Kawabata-Hansen phase function ($\langle\cos\alpha\rangle = 0.65$) and thus the similarity scaling factor ($1 - \langle\cos\alpha\rangle$) would yield estimates of $\tau_{\text{cl}} = 2.1$ and 7.1 for these two cases. Analysis of methane equivalent widths was repeated with the different phase functions. An example of the results is shown in Fig. 10b, where an open circle and open square are used to show how a particular point computed with the Kawabata-Hansen phase function is moved when the other phase functions are employed. In general, the effects are too small to affect our conclusions about the location of the deeper cloud or the CH_4 and NH_3 abundances.

On the other hand, observations which probe the skin of the atmosphere, such as those analyzed in Section 7, are more sensitive to the shape of the phase function (Tomasko *et al.*, 1978; Hansen,

[4] Other parameters were $I_c/F = 0.71$, $P_1 = 500$ mb, $P_2 = 630$ mb, $P_3 = 5$ bars, $\tilde{\omega}_{\text{cl}} = 1$ and $\tau_h = 0$.

1969). Therefore, the conclusions derived in Section 7 with regard to the vertical structure of the haze and cloud tops are subject to possible modification if the actual phase function is much different from the one employed, or if it differs greatly between the NTrZ and NEB.

9. Summary and discussion

In this section we summarize the information deduced on atmospheric composition and cloud structure, briefly discuss possible cosmogonical implications of the atmospheric composition and dynamical implications of the cloud and aerosol structure, and suggest future observations which would permit more precise analyses.

a. Atmospheric composition and cloud structure

Our approach was to start with the simplest models and modify these only as they proved inadequate to duplicate the key characteristics in the Jovian spectra of Woodman *et al.* (1979). In this way we proceeded through a hierarchy of models of increasing complexity, and were led to a model with substantial detail including two well-separated cloud regions and a haze region overlapping the upper cloud. This model requires 10 parameters, 6 to describe the two clouds and 4 to describe the haze region, and these parameters may differ between belt and zone regions. This is the *minimum* complexity required to describe the vertical structure of the portion of the atmosphere of Jupiter probed by the 3000–10 000 Å spectra, which is roughly the 100 mb–5 bar region. The fact that the model became more complex with each additional observation analyzed suggests that the actual situation is probably even more complicated than the 10-parameter model.

Nevertheless, we were able to obtain a number of quantitative conclusions which should survive even after new observations define a more detailed atmospheric structure. The main conclusions are summarized here.

1) CH_4 ABUNDANCE

The CH_4 abundance is $(1.8 \pm 0.4) \times 10^{-3}$ for $[CH_4]/[H_2]$. The error limit accounts for uncertainties in the cloud and haze structure. There is also possible systematic error, since there is a discrepancy in the laboratory and theoretical H_2 4-0 line strengths. We employed the smaller (laboratory) value; any increase will require a proportionate increase in the CH_4 abundance (Section 8). Based on current estimates of the solar composition (Table 1) the above methane abundance is $n = 2.0 \pm 0.4$ times greater than the carbon abundance in the atmosphere of the sun. Barring a large error in current knowledge of solar composition, carbon is definitely more abundant on Jupiter than on the sun.

Previous determinations of CH_4 abundances from measurements of spectra of reflected solar radiation range from less than $n = 1$ to $n = 5$–10 [cf. review by Wallace and Hunten (1978)]. However, the Jovian equivalent widths are accurately known, and we have shown that with appropriate scattering models the uncertainty in the CH_4 abundance is small. Our conclusion that $[CH_4]/[H_2] = (1.8 \pm 0.4) \times 10^{-3}$ is in reasonable agreement with the values reported by Smith and Greene (1978) based on photometry of satellite eclipses $(1.3 \pm 0.7) \times 10^{-3}$ and by Orton (1975) based on thermal infrared measurements (2.0×10^{-3}).

2) NH_3 ABUNDANCE

The NH_3 abundance is $(2.8 \pm 1.0) \times 10^{-4}$ for $[NH_3]/[H_2]$. The NH_3 abundance is subject to the same possible systematic error as the CH_4 abundance, due to the uncertainty in the H_2 4-0 line strength; if the laboratory value for that line strength is too small $[NH_3]$ will have to be increased proportionately. Based on current estimates of the solar composition, the above ammonia abundance is 1.5 ± 0.5 times greater than the nitrogen abundance in the atmosphere of the sun and the nitrogen overabundance on Jupiter may be as great as that for carbon. The indicated NH_3 abundance refers to the region beneath the level of possible ammonia condensation but above 3–5 bars; if NH_3 is depleted in this region by solution in H_2O clouds, the NH_3 abundance at greater depths is even larger.

Previous determinations of NH_3 abundance from measurements of spectra of reflected solar radiation cover a large range with most values significantly smaller than we have obtained (Sarangi and Margolis, 1978; Combes and Encrenaz, 1979). This reflects the fact that most NH_3 bands sample altitudes where NH_3 is depleted by condensation and/or photolysis. The bands in the 5000–6500 Å region are capable of yielding an accurate value for the NH_3 abundance beneath the ammonia clouds; previous discrepancies between abundances from the 5510 and 6450 Å NH_3 bands are primarily a result of overlap with CH_4 absorption which caused an underestimate of the true NH_3 equivalent width at 6450 Å (Section 6). Our conclusion that $[NH_3]/[H_2] = (2.8 \pm 1.0) \times 10^{-4}$ between 0.7 and 3 bars is consistent with the rough estimate 2×10^{-4} from microwave observations (Klein and Gulkis, 1978).

3) CLOUDS AND AEROSOLS

The basic cloud structure revealed by our analysis has two cloudy layers separated by a relatively

transparent region. The upper cloud layer occurs at a pressure level of several hundred millibars and the lower cloud top at 3–5 bars. Because the NH_3 abundance and Clausius/Clapeyron relation suggest NH_3 condensation in the region of the upper cloud, we assume that cloud is ammonia. The effective optical thickness of the upper cloud is ~10; because of possible horizontal inhomogeneities this is a lower limit for the mean optical thickness. The corresponding lower limit on the mass of condensed cloud material per unit area is $M \approx 10\ \rho r$ where ρ is the density of the cloud material and r the mean particle radius. The lower cloud is at an appropriate level to be H_2O, which may include ammonia in solution. We cannot definitely exclude the existence of NH_4SH or other clouds in the region between these two cloud layers, but such clouds must be sufficiently transparent to permit solar radiation in weak bands and the continuum to "see" to 3–5 bars.

There is also a more diffuse distribution of aerosols above the ammonia cloud region. These aerosols are basically scatterers ($\tilde{\omega} \approx 1$) of diameter $\gtrsim 1\ \mu$m. Their decreasing affect on the Jovian albedo with increasing wavelength is due to an increasing $\tilde{\omega}$ rather than a decreasing τ. They are therefore very different from the concept of Axel (1972) dust (size $\ll \lambda$, $\tilde{\omega} = 0$). We do not attempt to identify the composition of these aerosols, but the deduction about their size permits us to specify the wavelength-dependence of their absorption coefficient.

Absorption of solar radiation in the 3000–5000 Å region occurs in *both* the upper cloud region and the haze region above it. Thus there must be some constituent other than pure ammonia in the upper cloud region; this could be the same absorbing material as in the haze region. The "haze" and ammonia "cloud" regions are thus distinguished mainly by their optical densities; the haze region may include thin "cirrus" clouds and thicker localized clouds, and the denser cloud region must include an absorbing material in addition to ammonia.

We also obtain inferences about differences between the vertical cloud and aerosol structures of the NEB and NTrZ. These conclusions are based on second-order quantities, the ratio of belt and zone spectra, and they also require use of the center-to-limb variations in the spectra. The analysis may thus be influenced by factors such as horizontal inhomogeneities and variations in particle phase function, which cannot be determined from a single type of data at a single phase angle. Thus these inferences are not on as firm ground as those described above, and they should be reexamined with future data such as that described below. The basic conclusions from the ratio spectra are 1) the bulk of the above-cloud haze distribution is higher in the NTrZ than in the NEB, and 2) the main cloud tops are higher in the NEB than in the NTrZ. Since the distinction between the haze region (defined as $150 \lesssim P \lesssim 400$ mb) and the ammonia cloud region (defined as $400 \lesssim P \lesssim 700$ mb) is somewhat arbitrary, it is more rigorous to state this as: the optical thickness of particulates above a given pressure level $\tau(P)$ is greater in the zone than in the belt for the upper part of the haze region, but $\tau(P)$ is greater in the belt than in the zone for the upper part of the cloud region.

At face value the vertical structure of clouds and aerosols which we obtain is much different than most previous models. We believe, however, that our results are consistent with existing observational data. Our finding that there must be clouds in the ammonia cloud region (~400–700 mb) over both belts and zones differs from Terrile *et al.* (1978) and Orton and Ingersoll (1976) who suggest that there are no clouds in this layer over the belts; however, the data they employ are not definitive for this pressure range. The relative brightness of the zones perhaps suggests the absence of ammonia clouds over the belts, but the difference in reflectivity between belt and zone is only about 10% and this actually implies only modest differences in the transparency of the ammonia cloud region.

The relative transparency of the atmosphere which we find for the region 1–3 bars is in conflict with the presence of a massive NH_4SH cloud predicted on the basis of thermochemical equilibrium (Lewis and Weidenschilling, 1973), but not with any observational data of which we are aware. Our analysis only indicates that the 1–3 bar region is sufficiently transparent to permit penetration of a substantial amount of visible radiation to a lower cloud deck at 3–5 bars; thus there may be a significant amount of cloud material within the 1–3 bar region, which could contribute, for example, to the coloring of Jupiter. The cloud temperatures of <190, ~230 and ~300 K obtained by Terrile *et al.* (1978) are in good agreement with our model; the remote sensing technique we employ is not capable of resolving multiple cloud layers in the 3–6 bar region.

The indication we find for the top of the dense upper cloud deck extending to higher levels over the NEB than over the NTrZ should be reanalyzed with more appropriate data as described below. However, existing data do not seem to contradict this possibility. Polarization measurements have been interpreted in terms of higher cloud tops over the zones (Coffeen, 1974), but this data only indicates that the highest aerosols ($\tau \lesssim \frac{1}{2}$) are distributed higher over the zones than over the belts. Thus the polarization data are actually in good agreement with the aerosol distribution which we find for the region 150–400 mb. Thermal infrared measurements indicate higher effective temperature for the belts than for the zones (Ingersoll *et al.*, 1976),

but the difference is small and it is difficult to interpret this data in terms of cloud heights.

b. Implications for planetary formation and atmospheric dynamics

1) PLANETARY FORMATION

The molecular escape time from the major planets is much longer than the age of the universe even for hydrogen, so deviations of the present composition of these planets from solar composition are probably indicative of processes that occurred during planetary formation. Current models for the formation of the planets start with a gaseous nebula from which the sun may also have formed. Empirical information on the composition of the planets as a function of heliocentric distance can provide a crucial test of theories for how this nebula condensed to form the planets. In such considerations it is useful to group the important substances into three classes: permanent "gases" (primarily H_2 and He), "ices" (primarily CH_4, NH_3 and H_2O) and "rocks" (containing particularly Si, Fe and Mg). Based on the elemental composition of the solar atmosphere the mass percentages of these three groups are gases: ~98%; ices: ~1.4%; rocks: ~0.4%. Cameron (1973) has argued that the relative composition among the gases is fixed in the solar proportions, due to the absence of any known mechanism for bringing about separation. Relative proportions among the rocks, because of their nonvolatility, are also likely to be fixed at the solar values. Relative proportions among the ices and between the ices and rocks may vary depending on the temperatures in the solar nebula during accretion.

Our results indicate that CH_4 is enriched in the envelope of Jupiter, with an abundance $n(CH_4) \sim 2$ times larger than its solar abundance. Since NH_3 and H_2O are less volatile than CH_4, one would expect their abundances relative to the solar values to be at least as great. Our conclusion that $n(NH_3) \sim 1.5 \pm 0.5$ for $P \sim 1$–4 bars is consistent with $n(NH_3) \sim 2$ through the bulk of the envelope.

We infer from the CH_4 and NH_3 abundances that all of the ices and rocks exceed their solar abundance by at least a factor of 2, since it is very unlikely that Jupiter would have been assembled with a smaller efficiency for the less volatile material. This is consistent with current models for the interior of Jupiter which indicate a need for an overabundance of heavy elements relative to hydrogen and helium. The models of Stevenson and Salpeter (1976) involve ~10 Earth masses of heavy elements ($n \sim 2$–3), while those of Podolak and Cameron (1974) have about 50 Earth masses of heavy material.

Based on the weak methane band and hydrogen absorptions for the other major planets (Owen, 1976), we estimate $n(CH_4) \sim 2$ for Saturn and $n(CH_4) \sim 10$–20 for Uranus and Neptune. This should represent a lower limit on the amount of heavy elements on these planets. A lower limit on the mass of the protoplanetary nebula can be obtained by multiplying the mass of each major planet by $n(CH_4)$ and the mass of the terrestrial planets by 250, corresponding to the loss of all gases and ices. The resulting minimum mass for the primitive solar nebula is thus ~1500 Earth masses or ~0.5% of the solar mass.

These CH_4 and NH_3 abundances seem consistent with the following general concept for planetary formation by condensation and accretion of the planets from a cooling protoplanetary cloud of solar composition. Condensation and accumulation of rocky material and ices occurred with cooling of the cloud. The permanent gases, H_2 and He, were partially lost by the planetary system, either to the sun or removed outward by the solar wind. Jupiter and Saturn had sufficient mass to capture substantial amounts of the gases, with Uranus and Neptune able to capture smaller amounts.

The information on CH_4 and NH_3 abundances in the atmosphere of Jupiter could be interpreted very differently. For example, it is possible that the interior of the planet is less enriched in heavy elements than the atmosphere is; study of planetary formation is coupled with analysis of planetary interiors. More accurate and complete information on spectroscopic abundances for several planets would provide a useful constraint for models of planetary formation and planetary interiors.

Finally, we note that the apparent absence of the very thick NH_4SH clouds predicted for thermochemical equilibrium and solar composition could possibly be related to the process of planetary formation. For example, if S were bound up in FeS at the time of rock accretion at Jupiter, much of it may remain buried in the planetary core. This hypothesis seems conceivable since it appears to have been the case in the asteroid belt, as indicated by the composition of meteorites (Larimer, 1973), and would be consistent with the inability to observe H_2S spectroscopically (Prinn and Owen, 1976). However, J. Lewis and G. Sill (private communication) have pointed out that in such a case one would also expect P to be locked in the core, yet it is generously present in the atmosphere. The complete absence of NH_4SH clouds would pose another difficulty, since they are an attractive candidate for providing much of the coloring of Jupiter (Lewis, 1969; Lewis and Prinn, 1970; Prinn and Owen, 1976). Perhaps the most likely case is that some NH_4SH clouds are present, but they are sufficiently transparent to permit penetration of solar radiation of 3 ~ 5 bars. Resolution of these questions may

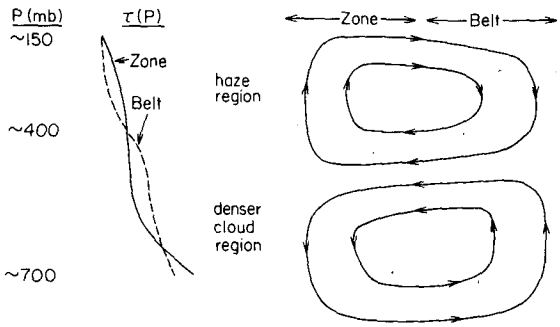

FIG. 25. A schematic indication of the optical depth $\tau(P)$ of aerosol and cloud particles above pressure level P. The designation of the interval between 700 mb and 400–500 mb as cloud region and the higher level as the above-cloud haze region is based on the substantially greater optical depth in the lower region, however the nomenclature for the two regions may be somewhat misleading as explained in the text. The mean meridional circulation sketched on the right is one conceivable dynamical explanation for the complicated variation with height of the relative optical depths in the NEB and NTrZ.

not be possible until the probe/orbiter spacecraft mission planned for 1985.

2) ATMOSPHERIC DYNAMICS

Accurate information on cloud properties and atmospheric composition should be useful in a number of ways for helping to analyze the dynamical state of the Jovian atmosphere. We focus here on the distribution of aerosol and cloud optical depth as a function of pressure, i.e., $\tau(P)$, and the vertical distribution of solar heating of the atmosphere.

A sketch of the $\tau(P)$ inferred in Section 7 for the NTrZ and NEB is included in Fig. 25. Throughout most of the upper haze region the optical thickness τ above pressure P is greater in the zone than in the belt, and the total optical thickness for the haze and cloud regions is greater for the zone than for the belt. But our interpretation of the ratio spectra of Woodman *et al.* (1979) suggests that there is a range of intermediate pressures, which we estimate as ~400–500 mb, for which the column optical depth is greater above the belt than above the zone. We describe this characteristic of $\tau(P)$ as indicating a higher cloud top in the belt, since the much larger optical thickness of the 400–700 mb region implies that it is the main cloud region. However, the distinction between the haze and cloud regions is somewhat arbitrary; for example, we showed that the material absorbing in the ultraviolet occurs in both haze and cloud regions (in both the NEB and NTrZ) and some ammonia clouds probably occur in the haze region as well as in the cloud region.

The usual dynamical interpretation has the zones as regions of rising motions and enhanced cloudiness [cf. review by Stone (1976)]. This is suggested by the observed zonal winds and the assumption that they are in geostrophic balance. If the $\tau(P)$ we have inferred from the ratio spectra of Woodman *et al.* (1979) is correct, it suggests that either the dynamical situation or the cloud physics is more complex than in this simple picture.

One conceivable dynamical explanation for the optical depth profiles is sketched on the right side of Fig. 25. This model would have rising motions in the belt in the main cloud region with sinking motion in the zone, but a reverse circulation above this with rising motion in the zone and sinking motion in the belt. In order for this picture to be consistent with observed zonal winds, the cloud features used for measuring the winds would need to be located in the upper cell (or tied to columnar features which penetrate through the 400–700 mb layer but are rooted below it). Features should be observable in both the upper haze and main cloud regions, so images with sufficient resolution should be useful for investigating the possibility of a double-cell circulation.

The absorption of solar energy in the blue and ultraviolet occurs in both the main cloud region and in the haze region above. In the visible and red most of the solar heating occurs within or below the main cloud region. The excess heating of the belts, because of their lower albedo, apparently must peak within or below the main cloud layer. This also could be interpreted as support for a double-cell circulation between belts and zones, with the excess heating in the belts contributing to driving a thermally direct circulation in (or just below) the main cloud region. Such a direct cell could contribute to bringing up colored material in the belts from deeper regions, while the cell in the opposite sense above could produce ammonia "cirrus" preferentially in the zones. The uncertainties in the profiles for both the excess heating and $\tau(P)$ would permit the lower cell to be at a somewhat greater pressure than indicated in Fig. 25.

Alternative explanations for the unusual $\tau(P)$ profile could be provided by considering the cloud and aerosol physics, but the current information for Jupiter seems too meager to warrant further speculation. It is not even known whether the UV-absorbing aerosols are stirred up from the deeper atmosphere, originate as photochemical products or have some other source.

The information that we have obtained about the atmospheric structure on Jupiter suggests that both the dynamics and cloud and aerosol physics may be very complex. There is also the implication that it will be difficult to decouple studies of dynamics from cloud and aerosol physics.

c. *Future observations*

The observations of Woodman *et al.* (1979) are of excellent quality for quantitative analysis. Some

improvements would be possible with better knowledge of viewing locations near the limb. Simultaneous measurements of H_2 equivalent widths are desirable. The single largest source of uncertainty in our analysis stems from the disparity in theoretical and laboratory values for the hydrogen quadrupole line strength (Section 8).

The best prospect for obtaining improved knowledge of the atmospheric structure with ground-based observations would involve a coordinated study over a broader spectral range. The 5 μm region and longer infrared wavelengths, if measured simultaneously with the 0.3–1 μm interval, would permit correlation of the pressure and temperature levels of cloud layers and study of particle size and composition from the spectral variation of optical thickness.

Two Voyager spacecraft currently approaching Jupiter for flyby reconnaissance include high-resolution imaging, infrared interferometry and ultraviolet photometry and polarimetry. These measurements will provide extensive information on the atmosphere, particularly the small-scale dynamics. Resolution at closest approach (~5 km) should permit measurement of some vertical structure, although this may be restricted to levels which we describe as the region of haze or thin "cirrus" clouds ($\lesssim$500 mb).

A more comprehensive analysis of the atmospheric structure and dynamics may be obtained with a combination of atmospheric probe and orbiter as planned by NASA for the 1982 launch of the Galileo mission to arrive at Jupiter in 1985. The probe will permit *in situ* sampling of atmospheric gaseous composition and cloud layers between ~100 mb and ~10 bars. The orbiter, with television camera and other remote sensing instrumentation, will perform observations supportive of and complementary to the probe measurements. One instrument (photopolarimeter/radiometer) on the orbiter will obtain photometric data such as we analyzed in this paper, but from a range of phase angles; since this instrument will also measure the radiation budget, atmospheric temperature profiles and polarization of scattered sunlight, it should be possible to analyze cloud and dynamical processes in detail.

Acknowledgments. We are extremely grateful to J. Woodman, W. Cochran and D. Slavsky for providing their paper prior to publication; W. Cochran generously answered many questions and supplied their data in forms most useful for analysis. T. Owen and B. Lutz also supplied data prior to publication and F. Herbert, A. Lacis and W. Wang provided subroutines used in our analysis. Valuable comments employed in revising our paper were obtained from, in addition to the above people, T. Encrenaz, L. Giver, J. Lewis, G. Orton, J. Pinto, G. Sill, P. Stone and W. Rossow.

REFERENCES

Allen, C. W., 1963: *Astrophysical Quantities*. Athlone Press, 291 pp.

Appleby, J. F., and D. J. van Blerkom, 1975: Absorption line studies of reflection from horizontally inhomogeneous layers. *Icarus*, **24**, 51–69.

Avery, R. W., J. J. Michalsky and R. A. Stokes, 1974: Variation of Jupiter's CH_4 and NH_3 bands with position on the planetary disk. *Icarus*, **21**, 47–54.

Axel, L., 1972: Inhomogeneous models of the atmosphere of Jupiter. *Astrophys. J.*, **173**, 451–467.

Beckman, J. E., 1967: The measurements of abundances in planetary atmospheres using an image intensifier and a solar spectrograph. *Planet. Space Sci.*, **15**, 1211–1218.

Bergstralh, J. T., 1973a: Methane absorption in the Jovian Atmosphere II. Absorption line formation. *Icarus*, **19**, 390–418.

——, 1973b: Methane absorption in the Jovian atmosphere I. The Lorentz half-width in the $3\nu_3$ band at 1.1 μm. *Icarus*, **19**, 499–506.

——, and J. S. Margolis, 1971: Recomputation of the absorption strengths of the methane $3\nu_3$ J-manifolds at 9050 cm^{-1}. *J. Quant. Spectrosc. Radiat. Transfer*, **11**, 1285–1287.

——, J. S., Margolis and J. W. Brault, 1978. Intensity and pressure shift of the $H_2(4,0)$ $S(1)$ quadruple line. *Astrophys. J.*, **224**, L39–L41.

Birnbaum, A., and J. D. Poll, 1969: Quadrupole tarnsitions in the H_2, HD and D_2 molecules. *J. Atmos. Sci.*, **26**, 943–945.

Cameron, A. G. W., 1973: Formation of the outer planets. *Space Sci. Rev.*, **14**, 383–391.

Carleton, N. P., and W. A. Traub, 1974: Observations of spatial and temporal variations of the Jovian H_2 quadrupole lines. *Exploration of Planetary System*. A. Woszezyk and C. Iwanisyewska, Eds., D. Reidel, 345–349.

Cochran, W. D., 1977: Jupiter: An inhomogeneous atmospheric model analysis of spatial variations of the H_2 4-0 $S(1)$ line. *Icarus*, **31**, 325–347.

——, J. Gelfand, and W. H. Smith, 1976: Spatially resolved spectroscopy of Jupiter, I. H_2 quadrupole 4-0 $S(1)$ line. *Astrophys. J.*, **207**, 639–645.

Coffeen, D. L., 1974: Optical polarization measurements of the Jupiter atmosphere at 103° phase angle. *J. Geophys. Res.*, **79**, 3645–3652.

Combes, M., and T. Encrenaz, 1979: A new method for the determination of abundance ratios in the outer planets—Application to Jupiter. *Icarus* (in press).

Danielson, R. E., and M. G. Tomasko, 1969: A two-layer model of the Jovian clouds. *J. Atmos. Sci.*, **26**, 889–897.

Dick, K. A., and U. Fink, 1977: Photoelectric absorption spectra of methane (CH_4), methane and hydrogen (H_2) mixtures, and ethane (C_2H_6). *J. Quant. Spectrosc. Radiat. Transfer*, **18**, 433–446.

Dicke, R. H., 1953: The effect of collisions upon the Doppler width of spectral lines. *Phys. Rev.*, **89**, 472–473.

Emerson, J. P., J. A. Eddy and G. A. Dulk, 1969: Hydrogen abundances in Jupiter's atmosphere. *Icarus*, **11**, 413–416.

Encrenaz, T., T. Owen and J. H. Woodman, 1974: The abundance of ammonia on Jupiter, Saturn and Titan. *Astron. Astrophys.*, **37**, 49–55.

Fink, U., and M. J. Belton, 1969: Collision narrowed curves of growth of H_2. *J. Atmos. Sci.*, **26**, 952–962.

——, D. C. Benner and K. A. Dick, 1977: Band model analysis of laboratory methane absorption spectra from 4500 to 10500 Å. *J. Quant. Spectrosc. Radiat. Transfer*, **18**, 447–457.

Galatry, L., 1961: Simultaneous effect of Doppler and foreign gas broadening on spectral lines. *Phys. Rev.*, **122**, 1218–1223.

Giver, L. P., 1978: Intensity measurements of the CH_4 bands in the region 4350 Å to 10,600 Å. *J. Quant. Spectrosc. Radiat. Transfer*, **19**, 311–322.

——, J. H. Miller and R. W. Boese, 1975: A laboratory atlas of the $5\nu_1$ NH_3 absorption band at 6475 Å with applications to Jupiter and Saturn. *Icarus*, **25**, 34–48.

Goody, R. M., 1964: *Atmospheric Radiation I. Theoretical Basis*. Oxford University Press, 436 pp.

Hansen, J. E., 1969. Absorption-line formation in a scattering planetary atmosphere: A test of van de Hulst's similarity relations. *Astrophys. J.*, **158**, 337–349.

——, 1971: Multiple scattering of polarized light in planetary atmospheres Part II. Sunlight reflected by terrestrial water clouds. *J. Atmos. Sci.*, **28**, 1400–1426.

——, and J. W. Hovenier, 1974: Interpretation of the polarization of Venus. *J. Atmos. Sci.*, **31**, 1137–1160.

——, and L. D. Travis, 1974: Light scattering in planetary atmospheres. *Space Sci. Rev.*, **16**, 527–610.

Herbert, F., 1974: Spectrum line profiles: A generalized Voigt function including collisional narrowing. *J. Quant. Spectrosc. Radiat. Transfer*, **14**, 943–951.

Herzberg, G., 1950: *Molecular Spectra and Molecular Structure I. Spectra of Diatomic Molecules*. van Nostrand, 658 pp.

Hunt, G. E., 1973a: Formation of spectral lines in planetary atmosphere IV. Theoretical evidence for structure of the Jovian clouds from spectroscopic observations of methane and hydrogen quadrupole lines. *Icarus*, **18**, 637–648.

——, 1973b: Interpretation of hydrogen quadrupole and methane observations of Jupiter and the radiative properties of the visible clouds. *Mon. Not. Roy. Astron. Soc.*, **161**, 347–363.

——, and J. T. Bergstralh, 1977: Interpretation of spatial and temporal variations of hydrogen quadrupole absorption in the Jovian atmosphere observed during the 1972 apparition. *Icarus*, **30**, 511–530.

Hunten, D. M., 1976: Atmospheres and ionospheres. *Jupiter*, T. Gehrels, Ed., University of Arizona Press, 22–31.

Ingersoll, A. P., G. Münch, G. Neugebauer and G. S. Orton, 1976: Results of the infrared radiometer experiment on Pioneers 10 and 11. *Jupiter*, T. Gehrels, Ed., University of Arizona Press, 197–205.

International Critical Tables of Numerical Data, 1928: Physics, Chemistry and Technology, Vol. 3, McGraw-Hill, 444 pp.

James, T. C., 1969: Calculations of collisional narrowing of the quadrupole lines in molecular hydrogen. *J. Opt. Soc. Amer.*, **59**, 1602–1606.

Kawabata, K., and J. E. Hansen, 1975: Interpretation of ground-based observations of the polarization of Jupiter. *Bull. Amer. Astron. Soc.*, **7**, 382–383.

Klein, M. J., and Gulkis, 1978: Jupiter's atmosphere: Observations and interpretation of the microwave spectra near 1.25 cm wavelength. *Icarus*, **35**, 44–60.

Lacis, A. A., 1975: Cloud structure and heating rates in the atmosphere of Venus. *J. Atmos. Sci.*, **32**, 1107–1124.

——, and W. C. Wang, 1979: Correlated k-distribution method for atmospheric radiation. To be submitted to *J. Atmos. Sci.*

Lambert, D. L., 1978: The abundances of the elements in the solar photosphere—VIII. Revised abundances of carbon, nitrogen and oxygen. *Mon. Not. Roy. Astron. Soc.*, **182**, 249–272.

Larimer, J. W., 1973: Chemical fractionations in meteorites—VII. Cosmothermometry and cosmobarometry. *Geochim. Cosmochim. Acta*, **37**, 1603–1623.

Lewis, J. S., 1969a: The clouds of Jupiter and the NH_3–H_2O and NH_3–H_2S systems. *Icarus*, **10**, 365–378.

——, 1969b: Observability of spectroscopically active compounds in the atmosphere of Jupiter. *Icarus*, **10**, 393–409.

——, and R. G. Prinn, 1970: Jupiter's clouds: structure and composition. *Science*, **169**, 472–473.

Lutz, B. L., 1979: Band strengths and curves-of-growth for the 5520 and 6475 Å bands of ammonia. Submitted to *Icarus*.

——, T. Owen and R. D. Cess, 1976: Laboratory band strengths of methane and their application to the atmospheres of Jupiter, Saturn, Uranus, Neptune and Titan. *Astrophys. J.*, **203**, 541–551.

——, —— and ——, 1977: The red bands of methane. *Bull. Amer. Astron. Soc.*, **9**, 537.

McKellar, A. R. W., 1974: The significance of pressure shifts for the interpretation of H_2 quadrupole lines in planetary spectra. *Icarus*, **22**, 212–219.

Maillard, J. P., M. Combes, Th. Encrenaz and J. Lecacheux, 1973: New infrared spectra of the Jovian planets from 12000 to 4000 cm^{-1} by Fourier transform spectroscopy. I. Study of Jupiter in the $3\nu_3$ CH_4 band. *Astron. Astrophys.*, **25**, 219–232.

Malkmus, W., 1967: Random Lorentz band model with exponential-tailed S^{-1} line-intensity distribution function. *J. Opt. Soc. Amer.*, **57**, 323–329.

Margolis, J. S., and K. Fox, 1969a: Studies of methane absorption in the Jovian atmosphere. I. Rotational temperature from the $3\nu_3$ methane band. *Astrophys. J.*, **157**, 935–943.

——, and ——, 1969b: Studies of methane absorption in the Jovian atmosphere. II. Abundance from the $3\nu_3$ methane band. *Astrophys. J.*, **158**, 1183–1188.

Morozhenko, A. V., and E. G. Yanovitskii, 1973: The optical properties of Venus and Jovian planets. I. The atmosphere of Jupiter according to polarimetric observations. *Icarus*, **18**, 583–592.

Orton, G. S., 1975: The thermal structure of Jupiter II. Observations and analysis of 8–14 micron radiation. *Icarus*, **26**, 142–158.

——, 1977: Recovery of the mean Jovian temperature structure from inversion of spectrally resolved thermal radiance data. *Icarus*, **32**, 41–57.

——, and A. P. Ingersoll, 1976: Pioneer 10 and 11 and ground-based infrared data on Jupiter: the thermal structure and He-H_2 ratio. *Jupiter*, T. Gehrels, Ed., University of Arizona Press, 206–215.

Owen, T., 1976: Chemical abundances in the atmospheres of the giant planets and their satellites. *Chemical Evolution of the Giant Planets*, C. Ponnamperuma, Ed., Academic Press, 49–58.

——, and H. P. Mason, 1968: The abundance of hydrogen in the atmosphere of Jupiter. *Astrophys. J.*, **154**, 317–326.

Penndorf, R., 1957: Tables of the refractive index for standard air and the Rayleigh scattering coefficient for the spectral region between 0.2 and 20.0μ and their application to atmospheric optics. *J. Opt. Soc. Amer.*, **47**, 176–182.

Podolak, M., and A. G. W. Cameron, 1974: Models of the giant planets. *Icarus*, **22**, 123–148.

——, 1975: Further investigations of Jupiter models. *Icarus*, **25**, 627–634.

Poll, J. D., and L. Wolniewicz, 1978: The quadrupole moment of the H_2 molecule. *J. Chem. Phys.*, **68**, 3053–3058.

Prinn, R. G., and T. Owen, 1976: Chemistry and spectroscopy. *Jupiter*, T. Gehrels, Ed., University of Arizona Press, 319–371.

Rank, D. H., U. Fink and T. A. Wiggin, 1966: Measurements on spectra of gases of planetary interest. II. H_2, CO_2, NH_3 and CH_4. *Astrophys. J.*, **143**, 980–988.

Ross, J. E., and L. H. Aller, 1976: The chemical composition of the sun. *Science*, **191**, 1223–1229.

Sarangi, S., and J. S. Margolis, 1978: A determination of Jovian ammonia abundance based on a 2 μm spectrum. *Icarus*, **36**, 330–333.

Sato, M., K. Kawabata and J. E. Hansen, 1977: A fast invariant imbedding method for multiple scattering calculations and an application to equivalent widths of CO_2 lines on Venus. *Astrophys. J.*, **216**, 947–962.

Scattergood, T., and T. Owen, 1977: On the sources of ultraviolet absorption in spectra of Titan and the outer planets. *Icarus*, **30**, 780–788.

Smith, D. W., and T. F. Greene, 1978: A stratospheric

methane abundance in Jupiter's South Temperate Zone. *Bull. Amer. Astron. Soc.*, **10**, 559.

Spinrad, H., and L. M. Trafton, 1963: High dispersion spectra of the outer planets. I. Jupiter in the visual and red. *Icarus*, **2**, 19–28.

Squires, P., 1957: The equatorial clouds of Jupiter. *Astrophys. J.*, **126**, 185–194.

Stevenson, D. J., and E. E. Salpeter, 1976: Interior models of Jupiter. *Jupiter*, T. Gehrels, Ed., University of Arizona Press, 85–112.

Stone, P. H., 1976: The meteorology of the Jovian atmosphere. *Jupiter*, T. Gehrels, Ed., University of Arizona Press, 586–618.

Strobel, D. F., 1973: The photochemistry of NH_3 in the Jovian atmosphere. *J. Atmos. Sci.*, **30**, 1205–1209.

Teifel, V. G., 1969: Molecular absorption and the possible structure of the cloud layers of Jupiter and Saturn. *J. Atmos. Sci.*, **26**, 854–859.

——, 1976: Morphology of molecular absorption on the disk of Jupiter. *Jupiter*, T. Gehrels, Ed., University of Arizona Press, 441–485.

Terrile, R. J., F. W. Taylor and R. Beer, 1978: New models of the clouds of Jupiter from radiometry and spectrometry in the 5 micron spectral window. *Bull. Amer. Astron. Soc.*, **10**, 562–563.

——, and J. A. Westphal, 1977: The vertical cloud structure of Jupiter from 5 μm measurements. *Icarus*, **30**, 274–281.

Tomasko, M. G., R. A. West and N. D. Castillo, 1978: Photometry and polarimetry of Jupiter at large phase angles. I. Analysis of imaging data of a prominent belt and a zone from Pioneer 10. *Icarus*, **33**, 558–592.

Trafton, L., 1972: Quadrupole H_2 absorption in the spectra of Jupiter and Saturn. *Bull. Amer. Astron. Soc.*, **4**, 359.

Trauger, J. T., M. E. Mickelson and L. E. Larson, 1978: Laboratory absorption strengths for the H_2 (4,0) and (3,0) S(1) lines. *Astrophys. J.*, **225**, L157–L160.

——, F. L. Roesler, N. P. Carleton and W. A. Traub, 1973: Observation of HD on Jupiter and the D/H ratio. *Astrophys. J.*, **184**, L137–L141.

Wallace, L., and D. M. Hunten, 1978: The Jovian spectrum in the region 0.4–1.1 μm: The C/H ratio. *Rev. Geophys. Space Phys.*, **16**, 289–319.

——, and G. R. Smith, 1977: The interpretation of Jovian methane absorptions. *Astrophys. J.*, **212**, 252–261.

Weidenschilling, S. J., and J. S. Lewis, 1973: Atmospheric and cloud structure of the Jovian planets. *Icarus*, **20**, 465–476.

West, R. A., 1979: Spatially resolved methane band photometry of Jupiter. II. Analysis of the South Equatorial Belt and South Tropical Zone reflectivity. *Icarus*, **38**, 12–33.

Woodman, J. H., W. D. Cochran, and D. B. Slavsky, 1979: Spatially resolved reflectivities of Jupiter during the 1976 opposition. *Icarus*, **37**, 73–83.

——, L. Trafton and T. Owen, 1977: The abundance of ammonia in the atmospheres of Jupiter, Saturn, and Titan. *Icarus*, **32**, 314–320.

Zabriskie, F., 1962: Hydrogen content of Jupiter's atmosphere. *Astron. J.*, **67**, 168–170.